BEILSTEIN JOURNAL OF NANOTECHNOLOGY

Converging technologies for nanobio-applications

Edited by Witold Łojkowski and Dariusz Smoleń

Imprint

Beilstein Journal of Nanotechnology
www.bjnano.org
ISSN 2190-4286
Email: journals-support@beilstein-institut.de

The *Beilstein Journal of Nanotechnology* is published by the Beilstein-Institut zur Förderung der Chemischen Wissenschaften.

Beilstein-Institut zur Förderung der Chemischen Wissenschaften
Trakehner Straße 7–9
60487 Frankfurt am Main
Germany
www.beilstein-institut.de

BEILSTEIN JOURNAL OF NANOTECHNOLOGY

Nanobioarchitectures based on chlorophyll photopigment, artificial lipid bilayers and carbon nanotubes

Marcela Elisabeta Barbinta-Patrascu[1], Stefan Marian Iordache[*2], Ana Maria Iordache[2], Nicoleta Badea[3] and Camelia Ungureanu[*3]

Full Research Paper

Open Access

Address:
[1]Department of Electricity and Magnetism, Solid-State Physics and Biophysics, Faculty of Physics, University of Bucharest, 405 Atomistilor Street, P.O. Box MG-11, Bucharest-Magurele, 077125, Romania, [2]3Nano-SAE Research Centre, Faculty of Physics, University of Bucharest, P.O. Box MG-38, Bucharest-Magurele, 077125, Romania and [3]Department of General Chemistry, Faculty of Applied Chemistry and Materials Science, University Politehnica of Bucharest, 1–7 Polizu Street, 011061, Bucharest, Romania

Email:
Stefan Marian Iordache[*] - stefan@3nanosae.org;
Camelia Ungureanu[*] - ungureanucamelia@gmail.com

* Corresponding author

Keywords:
antibacterial activity; antioxidant properties; artificial lipid bilayers; carbon nanotubes; chlorophyll

Beilstein J. Nanotechnol. **2014,** *5,* 2316–2325.
doi:10.3762/bjnano.5.240

Received: 27 August 2014
Accepted: 12 November 2014
Published: 02 December 2014

This article is part of the Thematic Series "Converging technologies for nanobio-applications".

Guest Editor: W. Lojkowski

Abstract

In the last decade, building biohybrid materials has gained considerable interest in the field of nanotechnology. This paper describes an original design for bionanoarchitectures with interesting properties and potential bioapplications. Multilamellar lipid vesicles (obtained by hydration of a dipalmitoyl phosphatidylcholine thin film) with and without cholesterol were labelled with a natural photopigment (chlorophyll *a*), which functioned as a sensor to detect modifications in the artificial lipid bilayers. These biomimetic membranes were used to build non-covalent structures with single-walled carbon nanotubes. Different biophysical methods were employed to characterize these biohybrids such as: UV–vis absorption and emission spectroscopy, zeta potential measurements, AFM and chemiluminescence techniques. The designed, carbon-based biohybrids exhibited good physical stability, good antioxidant and antimicrobial properties, and could be used as biocoating materials. As compared to the cholesterol-free samples, the cholesterol-containing hybrid structures demonstrated better stability (i.e., their zeta potential reached the value of −36.4 mV), more pronounced oxygen radical scavenging ability (affording an antioxidant activity of 73.25%) and enhanced biocidal ability, offering inhibition zones of 12.4, 11.3 and 10.2 mm in diameter, against *Escherichia coli, Staphylococcus aureus* and *Enterococcus faecalis*, respectively.

Introduction

The "nanoworld" has long fascinated scientists due to the interesting properties that small-dimensional objects provide (as compared to their bulk counterparts) and the design of bionanohybrids has gained considerable interest in the fields of nanotechnology and biomedicine [1-3]. Special attention has been paid to biomimetic membranes that convey biocompatibility to the hybrid materials [4-7].

One of the building blocks used to construct nanomaterials are carbon nanotubes (CNTs), which are allotropes of carbon with a unique nanostructure consisting of graphene sheets (layers of sp^2-hybridized carbon atoms, perfectly hexagonally packed in a honeycomb network) rolled up into tubular shapes with a very large length/diameter ratio. This structure gives the unusual properties of CNTs such as: high mechanical strength (due to C–C sp^2 bonds, which is one of the strongest bonds), flexibility without breakage or damage, high elasticity, good electrical conductivity, and chemical stability. These cylindrical graphene nanotubes are considered one of the most attractive nanomaterials. Applicability of CNTs in the biomedical field is complicated as they are completely insoluble in all solvents and are present as bundles. Thus, they have a tendency to aggregate due to van der Waals forces, π–π stacking and hydrophobic interactions among individual CNTs, making them difficult for characterization, handling, and analytical investigations. These problems can be overcome by functionalization [8,9].

Carbon nanotubes are widely used in the biomedical field due to their unusual properties and because CNT toxicity occurs only in the pristine form and in very high doses [10,11]. Kam et al. [12] observed functionalized single-walled carbon nanotubes (f-SWCNTs, 0.05 mg/mL) internalized inside hamster ovary cells without toxicity. Immature dendritic cells incubated with doses of SWCNTs up to 100 μg/mL had no effect on their functionality and viability [13]. Many scientific papers report that oral administration of both pristine and f-CNTs do not induce toxicity in mice [14-17].

On the other hand, biocoating SWCNTs with biomolecules such as phospholipids conveys biocompatibility and less toxicity to carbon nanotubes. Moreover, SWCNTs are characterized by less accumulation in body as compared to multi-walled carbon nanotubes [18]. Bianco et al. [19] showed that carbon nanotube biofunctionalization lead not only to the improved solubility and biocompatibility of CNTs, but also transformed them into platforms for biomedical applications. Carbon nanotubes are generally considered biocompatible and of low toxicity for biomedical purposes. To this regard, Firme and Bandaru [11] reviewed the applications of carbon nanotubes to biological systems and highlighted the possibility that cells have cascade reactions that can resist the toxicity induced by CNTs. Ghafari et al. [20] observed that CNTs can be actively ingested and excreted from cells without any observable toxicity effects (e.g., as in case of *Tetrahymena thermophila* bacteria). Furthermore, Kagan et al. [21] pointed out that certain enzymes such as myeloperoxidases can degrade carbon nanotubes, breaking them down into water and carbon dioxide.

CNTs are largely used as drug delivery vehicles, showing potential in targeting specific cancer cells [18] with a necessary dosage lower than conventional drugs, without harming healthy cells and significantly reduced side effects. Another interesting property of carbon nanotubes is their antioxidant activity, which has been exploited in the preparation of anti-aging cosmetics and sunscreen creams to protect skin against free radicals formed by the body or by UV sunlight [10].

The goal of this work is to achieve antioxidant and antibacterial bionanomaterials based on liposomes and carbon nanotubes, which could open new perspectives for biomedical and biotechnological applications. The increased interest in use of phospholipids is due to the fact that they are basic structural components of biomembranes and artificial lipid membranes (liposomes). Liposomes are spherical, soft-matter vesicles composed of one or more lipid membranes (called lamellae) separated by aqueous compartments [22], with the structure of their lipid bilayers resembling that of cell membranes.

In this work, we present the preparation of complex biocomposites based on liposomes and carbon nanotubes. Chlorophyll *a* is used as a molecular sensor (or as a spectral marker in spectroscopic methods) for rapid monitoring of the preparation of the complex biohybrid materials, which provides evidence of the interaction of CNTs with the versatile models of biomembranes for possible biomedical applications. This work encompasses the research stage with the design, preparation and characterization techniques needed for monitoring these biomaterials, and presents new interdisciplinary aspects involving concepts of biochemistry, biophysics, microbiology, nanotechnology, colloid and supramolecular chemistry, and materials science. The biophysical studies on interaction between the nanostructures and amphiphilic molecules presented here allow for an understanding the structure of molecular assemblies and facilitate the full exploitation of the bioapplicability potential of the resulting bionanomaterials.

Experimental

Materials

Luminol (5-amino-2,3-dihydro-1,4-phthalazinedione), KH_2PO_4, Na_2HPO_4, Tris (tris(hydroxymethyl)aminomethane), HCl, and

H_2O_2were purchased from Merck (Germany). Methanol (99.9%), SWCNTs and the lipids used for the liposome preparation (dipalmitoylphosphatidylcholine, DPPC and cholesterol, Chol) were supplied from Sigma-Aldrich (Germany).

The antimicrobial activity was tested against human pathogenic bacteria such as *Staphylococcus aureus* ATTC 25923, *Escherichia coli* ATCC 8738, and *Enterococcus faecalis* ATCC 29212. The bacterial strains were grown in Luria Bertani Agar (LBA) plates at 37 °C with the following composition: peptone (Merck, 10 g/L), yeast extract (Biolife, 5 g/L), NaCl (Sigma-Aldrich, 5 g/L) and agar (Fluka, 20 g/L).

Synthesis

Liposome preparation

The hydration method [22] of a thin DPPC film was used to obtain two kinds of multilamellar lipid vesicles (MLVs, 0.5 mM) with and without cholesterol in the artificial lipid bilayers (DPPC:Chol molar ratio = 4:1), which were suspended in a safe bio-dispersant of phosphate buffer solution (PB, KH_2PO_4–Na_2HPO_4, pH 7.4). Chlorophyll *a* (Chl*a*), a natural antioxidant porphyrin, was extracted from spinach leaves according to the Strain and Svec method [23]. Considering its antioxidant properties [24,25] and spectral features, this photopigment was chosen and inserted (Chl*a*:lipid molar ratio = 1:100) into the both types of liposomes: Chl*a*–DPPC–MLVs (sample V1) and Chl*a*–Chol (20%)–DPPC–MLVs (sample V2) as described previously [4-6]. A summary of the sample abbreviations used in this work are presented in Table 1.

Table 1: The sample composition and abbreviations for the biostructures prepared in this work.

Sample description	Sample name
Chl*a*–DPPC–MLVs	V1
Chl*a*–Chol–DPPC–MLVs	V2
Chl*a*–DPPC–MLVs/CNTs hybrid	V3
Chl*a*–Chol–DPPC–MLVs/CNTs hybrid	V4

Preparation of the liposome/SWCNT biocomposites

Small aliquots of a previously sonicated SWCNT stock suspension (0.9 mg/mL, in PB pH 7.4) were added to a liposome suspension and the resulting mixture was subjected to ultrasound treatment (Hielser titanium probe sonicator, UP 100H, 15 min with breaks). Figure 1 shows the schematic representation of the ultrasound-mediated biohybrid preparation resulting in two types of biocomposites: Chl*a*–DPPC–MLVs/CNTs hybrid (sample V3) and Chl*a*–Chol–DPPC–MLVs/CNTs hybrid (sample V4). Due to the photosensitivity of the samples, all the experiments were carried out in dark.

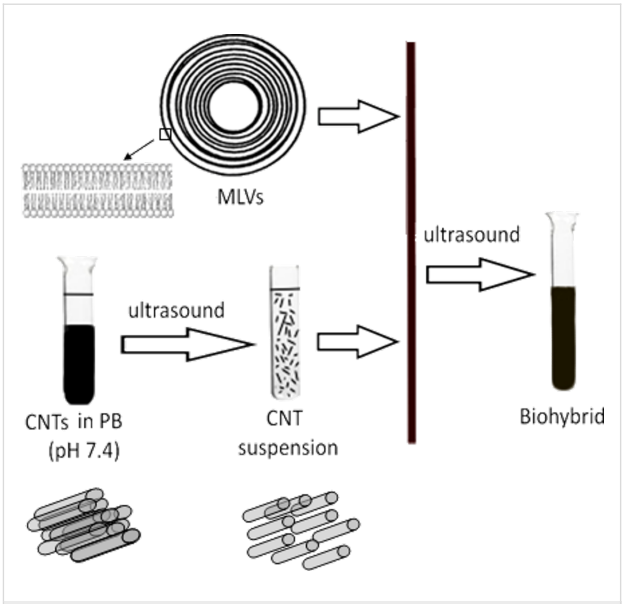

Figure 1: Schematic representation of the biohybrid preparation.

Characterization methods

Absorption spectroscopy

The absorption spectra were recorded using a double beam UV–vis spectrophotometer (M400, Carl Zeiss, Germany) in range of 200–800 nm, with a resolution of 1 nm using a 1 nm slit width and a 0.3 nm/s scan rate.

Fluorescence analysis

The fluorescence emission spectra of Chl*a* in liposomes and hybrid structures were collected on a Perkin-Elmer, LS55 fluorescence spectrometer. The samples were excited with 430 nm excitation light.

Fluorescence anisotropy measurements were carried out on the same spectrofluorometer (using parallel and perpendicular polarizers) fitted with a biokinetic accessory, affording continuous monitoring of the temperature in the cuvette and magnetic stirring of the suspensions of liposomes and biohybrids. Slit widths of 7.5 and 4 nm were used for the excitation and emission window, respectively. The anisotropy was calculated as the mean value of seven independent measurements, at a specified temperature, using the equation:

$$r = [(I_{vv} - GI_{vh}) / (I_{vv} + 2GI_{vh})], \quad (1)$$

where I represents the relative fluorescence intensity, the subscripts v and h represent the vertical and horizontal orientation of the excitation and emission polarizers, respectively, and G, the instrumental grating factor, is defined as the ratio of the sensitivities of the detection system for vertically and horizontally polarized light [26].

Zeta potential determination

The measurement of the electrokinetic potential is used to assess the charge stability of a disperse system. The measurement of the zeta potential (ZP) was realized by use of a Zetasizer Nano ZS (Malvern Instruments Ltd., U.K.). The ZP is measured by applying an electric field across the analyzed aqueous dispersion. All measurements were performed in triplicate.

Dynamic light scattering (DLS) measurements

The size of the liposomes represented by the hydrodynamic diameter, $Z_{average}$ (the particle diameter plus the double layer thickness) was measured using DLS (Zetasizer Nano ZS, Malvern Instruments Ltd., U.K.) at 25 °C at a scattering angle of 90°. The average diameters (based on the Stokes–Einstein equation) and the polydispersity index (PDI, indicating the width of the size distribution) were obtained from 3 individual measurements using an intensity distribution.

Atomic force microscopy (AFM)

AFM images were recorded on an integrated platform, AFM/SPM (NTEGRA Prima, NT-MDT, USA) in semi-contact mode (scanning area range 1.2 × 1.2 μm^2) using an NSG01 cantilever with a typical radius of curvature of 10 nm. All AFM measurements were obtained on samples deposited on Si plate substrates.

Chemiluminescence (CL) assay

The in vitro antioxidant activity of the samples was determined by chemiluminescence (CL) assay using a chemiluminometer (Turner Design, TD 20/20, USA). A wide range of oxygen free radicals (reactive oxygen species, ROS) [27,28] was formed by a generator system based on H_2O_2 in an alkaline buffer solution (Tris·HCl, pH 8.6) mimicking an oxidative stress. Luminol was introduced as light amplifier in this system in order to increase the detection sensitivity of activated oxygen species. The antioxidant activity (*AA*, %) was calculated as a percentage of free radical scavenging of each sample using:

$$AA = [(I_0 - I) / I_0] \cdot 100\%, \quad (2)$$

where I_0 is the maximum CL intensity for a standard sample at t = 5 s, and I is the maximum CL intensity for a sample at t = 5 s [29]. Three measurements were performed for each sample in order to accurately evaluate the antioxidant activity.

Antibacterial assay

The antibacterial activity of the samples was tested against Gram-positive and Gram-negative bacteria from the American Type Culture Collection (ATCC). In the present study three bacterial strains were used for the antibacterial assay: *Staphylococcus aureus* (ATCC 6538), *Enterococcus faecalis* (ATCC 29212) and *Escherichia coli* (ATCC 8738). The microorganisms used in this study were selected because of their clinical importance in terms of medical and food applications [30-35]. The bacterial strains were cultivated in a tube containing a Luria Bertani (LB) medium as reported recently by Ansari et al. [36]. The Kirby–Bauer disk-diffusion method was performed to determine the antibacterial potential of the samples [37]. Sterile LBA plates were prepared by pouring the sterilized media into sterile Petri plates (diameter = 90 mm) under aseptic conditions.

The sensitivity of the microorganism species to the biohybrids prepared was determined by measuring the size of inhibitory zones (including the diameter of sample) on the agar surface around the sample with a minimum cut-off value set at 8 mm. The inhibition zone was measured and expressed in millimetres. In this study triplicate plates were prepared for each sample and bacterial strain. The mean zone of inhibition was calculated with a standard deviation procedure. The data were presented as mean ± standard deviation (SD). The SD was calculated as the square root of variance using the STDEV function in Excel 2010.

Results and Discussion

Spectral characterization of nanobioarchitectures

The formation of DPPC, multilamellar lipid vesicles was confirmed by DLS. The size distribution profile (Figure 2) was bimodal for both types of liposomes.

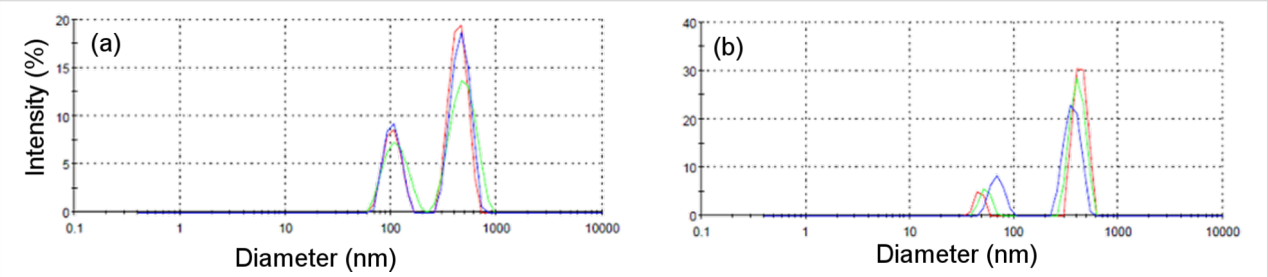

Figure 2: The size distribution profile of (a) Chl*a*–DPPC–MLVs (sample V1) and (b) Chl*a*–Chol–DPPC–MLVs (sample V2).

From these results, one can see that the cholesterol-containing artificial lipid bilayers have smaller dimensions ($Z_{average}$ = 567.6 ± 116.2; PDI = 0.322 ± 0.067) than liposomes without cholesterol ($Z_{average}$ = 609.8 ± 112.7; PDI = 0.397 ± 0.053).

Chl*a* inserted into the lipid bilayers of liposomes was used as a spectral sensor to monitor the events occurring in the biomimetic membranes. The visible absorption spectra of the samples were normalized versus the absorption at the maximum peak around 670 nm (see Figure 3).

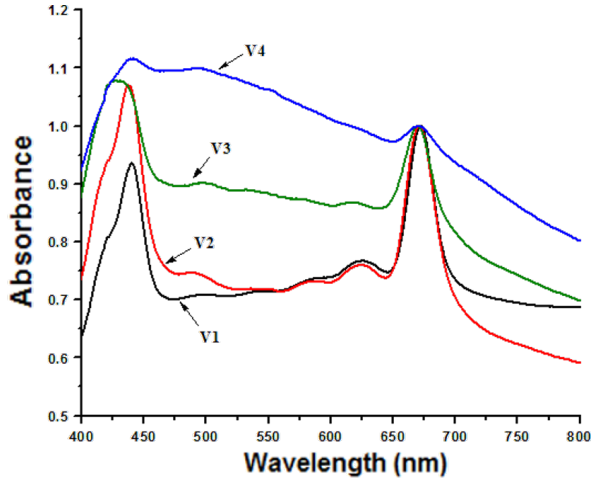

Figure 3: The VIS absorption spectra of Chl*a* in biomimetic membranes and in bio-hybrids.

The spectral fingerprint of the Chl*a* sensor consists of specific absorption bands: in the red region (an intense peak at about 670 nm) and in the blue region (Soret band) of the electromagnetic spectrum.

In the case of cholesterol-free samples, the position of the Chl*a* absorption maximum was slightly blue-shifted (from 672 to 670 nm). On the contrary, no change in the location of the Chl*a* peaks in the cholesterol-containing samples (the red absorption band occurred at 671 nm) was observed, because the cholesterol enhances the membrane stability and restricts the lipid mobility [38].

The architecture of the biomimetic membranes changed after interacting with the carbon nanotubes, evident from the changes in the Soret band. Fluorescence spectroscopy was used in order to gain further information on this interaction at the molecular level. Figure 4 and Figure 5 were obtained by excitation at λ = 430 nm and the emission fluorescence maximum of Chl*a* incorporated in biomimetic membranes and in biohybrids was at 680 nm.

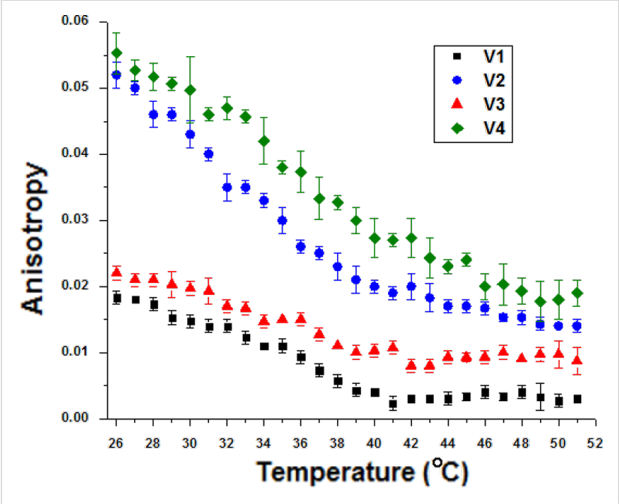

Figure 4: The thermal behavior of the emission anisotropy of Chl*a* in the samples.

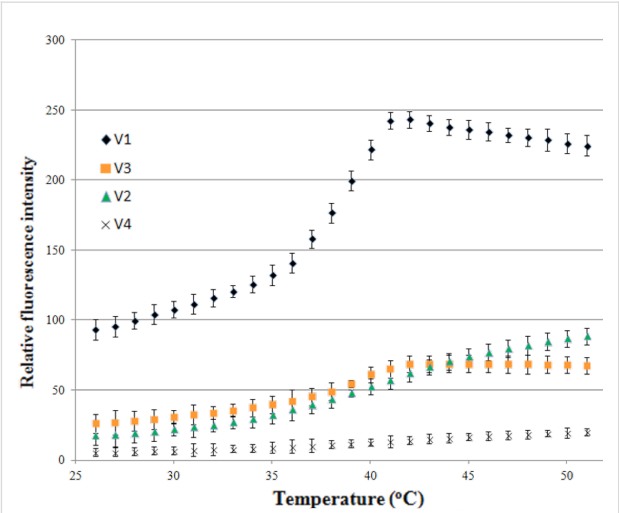

Figure 5: The variation with temperature of the maximum of the relative fluorescence intensity of Chl*a* in the samples.

The fluorescence anisotropy of biohybrids is greater than that of liposomes (Figure 4), thus Chl*a* sensed a more rigid environment. This makes Chl*a* beneficial regarding its involvement in non-covalent interactions between lipid vesicles and SWCNTs.

In the case of the biohybrids, the variation with temperature of the maximum of relative fluorescence intensity of Chl*a* embedded in artificial lipid bilayers was much slower as compared with the liposomes alone (see Figure 5). This is due to the presence of carbon nanotubes, which reduces the motion of Chl*a*, which is a result supported by the evolution of the Chl*a* emission anisotropy with temperature. A dramatic quenching of the Chl*a* fluorescence was observed in the presence of SWCNTs due to a more efficient energy transfer between the

Chl*a* molecules incorporated in liposomes (ordered along SWCNTs) as a result of interaction with the carbon nanotube sidewall. These findings are in agreement with our previous studies [4,5].

As can be seen in both Figure 4 and Figure 5, the liquid crystal phase of biomimetic membranes (above 41 °C) exhibits low anisotropy and high fluorescence emission intensity due to an increase in the lipid bilayer mobility and hence the chlorophyll has the possibility to move and to minimize the energy transfer leading to fluorescence quenching.

In the gel phase of the artificial lipid bilayers (below 41 °C), high values of anisotropy and low emission fluorescence intensities of Chl*a* inserted into lipid membranes can be observed due to the fluorescence quenching of Chl*a* in a more rigid environment.

The cholesterol-containing samples exhibited high anisotropy and the fluorophore motion is more restricted in this case, that is, Chl*a* senses a more ordered environment. This is due to the presence of cholesterol which induces high order and rigidity in lipid membranes [26,38]. On the other hand, the low fluorescence intensity in the samples with cholesterol could be explained by their small size as compared to the samples without cholesterol (see Figure 2). This leads to fluorescence quenching due to the efficient energy transfer between chlorophyll molecules, which are closer in small vesicles.

Morphological characterization of biohybrid architectures

Figure 6 shows a partial exfoliation of CNT bundles in the case of free-cholesterol biohybrids (sample V3). On the contrary, the cholesterol-containing, carbon-based biohybrids (sample V4) proved to be more effective in CNT dispersion. In this case, the AFM analysis revealed a lipid coating around the carbon nanotubes that prevents their aggregation; spherical-shaped profiles of liposomes could be observed along and near the carbon nanotubes. Thus, a carbon nanotube network was formed by the cross-linking of CNTs via liposomes with islands of lipid vesicles. This proves that the bionanocomposite undergoes self-assembly in an ordered fashion (Figure 6b) and not just simple agglomeration of particles (Figure 6a).

Performance testing of bionanoarchitectures

Evaluation of the physical stability of liposome/CNT biohybrids

As known from the scientific literature, one of the key factors that determines the physical stability of emulsions and suspensions is the particle charge, which is quantified with the ZP. The ZP is a physical property measured via the electrophoretic mobility of the particles in an electric field [39]. A minimum ZP value of ±30 mV is necessary to ensure the stability of a suspension [40,41]. The physical stability of the biohybrids was rapidly estimated in terms of the ZP. The samples, suspended in PB (pH 7.4) as a biodispersant, carry a negative electric charge. Therefore, if the particles have a large, negative ZP value resulting in high electrostatic repulsion, the dispersion will be stable. The liposomes alone have a low ZP value, thus exhibiting short-term stability, and the repulsive forces are very weak to prevent the particles from coming together. The cholesterol-containing lipid vesicle suspensions, having a ZP value of −19.7 mV, are more stable than vesicles without cholesterol (ZP = −17.2 mV). The carbon-based biohybrids exhibited high stability, possessing a large negative value of the ZP. The cholesterol-containing hybrids were even more stable (ZP = −36.4 mV) than the cholesterol-free biohybrids (ZP = −31.7 mV). Figure 7 presents the stability evaluation of the cholesterol-containing biohybrid (sample V4) by zeta potential distribution. We observed that cholesterol-loaded

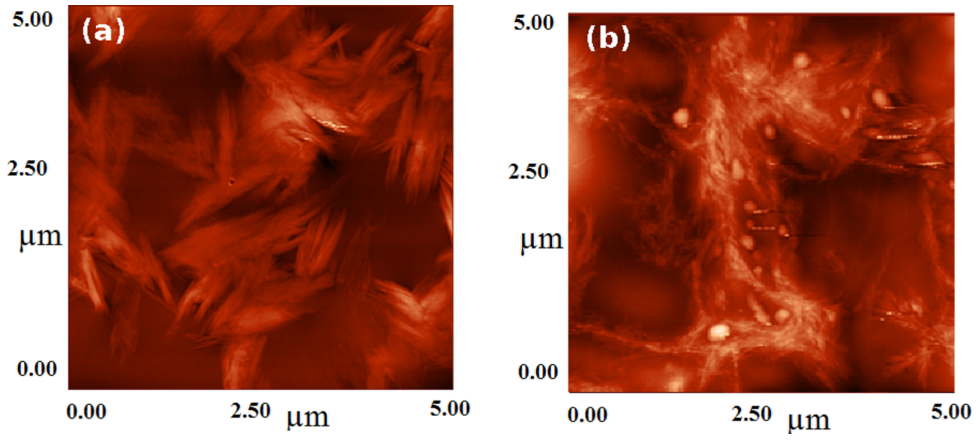

Figure 6: AFM micrographs of nanobioarchitectures without (a) and with (b) cholesterol.

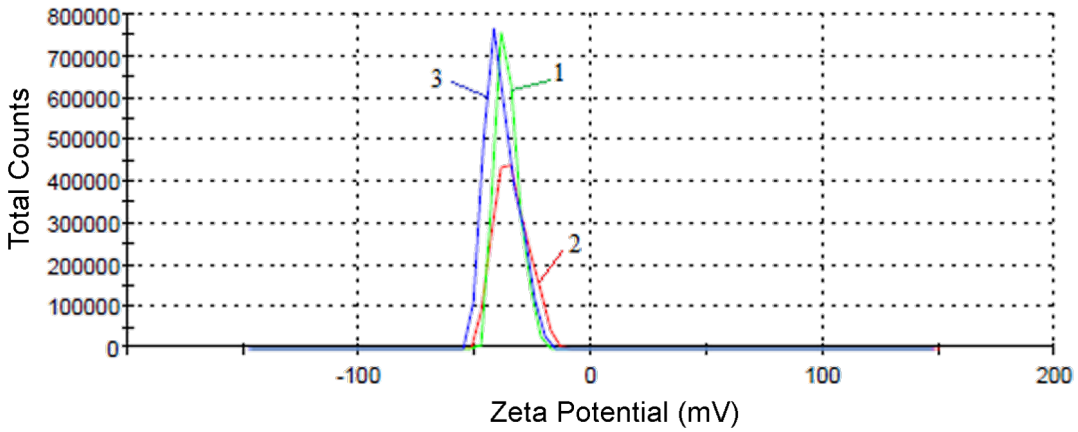

Figure 7: Evaluation of the cholesterol-containing biohybrid (sample V4) stability from the zeta potential distribution, where the ZP was performed in triplicate and the indices 1, 2 and 3 refer to each measurement.

samples form more stable structures than the samples without cholesterol.

The antioxidant behavior of the samples

In this paper, the chemiluminescence technique was used to estimate the capacity of the SWCNTs/liposomes hybrids to scavenge free radicals. The oxygen radical scavenging ability of the samples was evaluated in terms of antioxidant activity (see Equation 2 in the section Characterization methods). The antioxidant profile of the liposomes and bio-composites displayed in Figure 8 reveals that nanocarbon-based biohybrids possess strong ROS scavenging capacity.

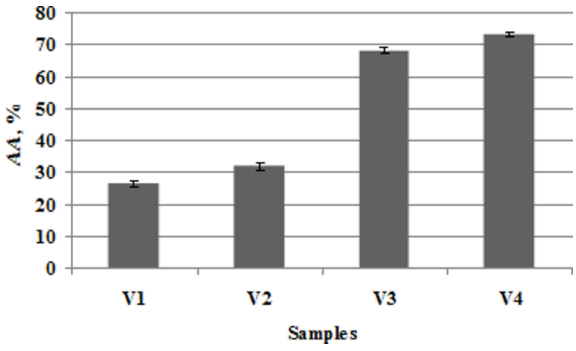

Figure 8: Antioxidant activity of the samples.

The lipid vesicles alone presented low levels of antioxidant activity (25.9% for V1 and 33.1% for V2), but the addition of SWCNTs to liposomal suspensions resulted in biohybrids with enhanced values of antioxidant activity (68.2% for V3 and 73.25% for V4). The antioxidant behavior of liposomes is due to their chlorophyll content, as it is a photopigment known to possess antioxidant properties [24,25].

One explanation for the good antioxidant action of these SWCNTs/liposomes hybrid systems is that the strong potency of these biohybrids is mainly due to the presence of carbon nanotubes. Although the study of the free-radical scavenging properties of CNTs is an emerging area of nanotechnology, only a few research papers have reported the antioxidant nature of SWCNTs [42,43]. According to some reports [44,45], the free radical scavenger property of CNTs could be attributed to their high electron affinity, suggesting also that ROS may be "grafted" at the CNT surface via radical addition to the nanotube framework. Our previous studies also demonstrated that the presence of SWCNTs in biohybrid materials enhanced their antioxidant properties [4,5,46]. Another more simple explanation is that the chlorophyll embedded in liposomes could convey the antioxidant properties. Finally, the good dispersion state of these hybrids (emphasized by AFM analysis and ZP measurements) could afford more reaction centers that might enhance the capacity of ROS scavenging.

The most potent biohybrids against oxidative attack of free radicals were found to be those with cholesterol (see sample V4), likely due to their better degree of SWCNT dispersibility and their high physical stability as compared to the cholesterol-free biohybrids (sample V3).

Antimicrobial activity of samples

The antimicrobial investigations were performed on Gram-negative (*Escherichia coli*) and Gram-positive (*Staphylococcus aureus*, *Enterococcus faecalis*) bacteria. Phosphate buffer solution (pH 7.4) was the negative control for all the samples.

The liposomes alone (samples V1 and V2) showed weak antibacterial activity (see Figure 9), offering inhibition zone diameters in the range of 5.0–6.1 mm. However, their biohy-

brids with carbon nanotubes exhibited enhanced biocidal features due to the presence of SWCNTs, which are known to possess antimicrobial properties [47,48]. Kang et al. [49] pointed out that cell membrane damage resulting from direct contact with carbon nanotubes is the most plausible mechanism leading to bacterial cell death.

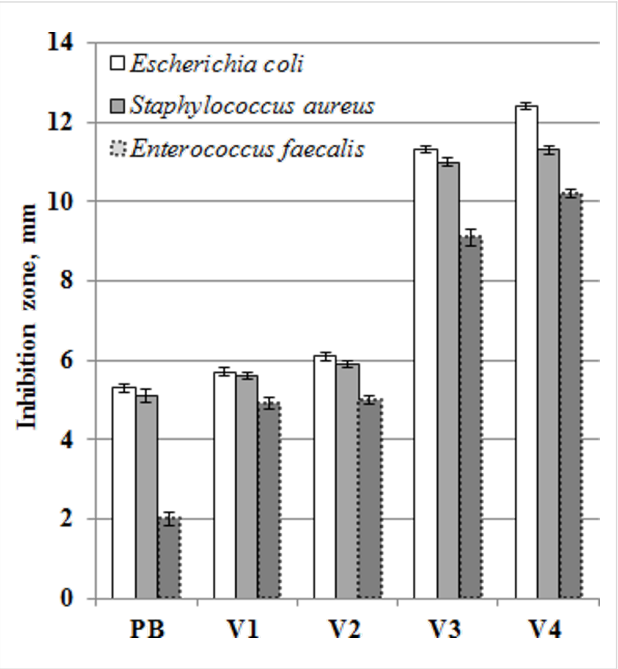

Figure 9: Antibacterial activity of the samples.

Our results showed that small amounts of SWCNTs were enough to achieve high antimicrobial potency (see samples V3 and V4). The cholesterol-free, carbon-based biohybrids (V3) proved to be effective antibacterial materials, presenting inhibition zone diameters of 11.3, 11.0 and 9.1 mm against *Escherichia coli*, *Staphylococcus aureus* and *Enterococcus faecalis*, respectively. On the other hand, the hybrids based on cholesterol-containing biomimetic membranes (V4) have been proven to be the most potent antibacterial material, offering even greater inhibition zones (12.4, 11.3 and 10.2 mm against *Escherichia coli*, *Staphylococcus aureus* and *Enterococcus faecalis*, respectively). An explanation of this behavior of sample V4 compared to sample V3 is a greater degree of dispersibility (according to ZP values and AFM results), which allows for better contact with the bacterial cell. Through this interaction, biomimetic membranes fuse with the natural ones, thus damaging their integrity.

Conclusion

This paper describes an original design of bionanoarchitectures with interesting properties and potential applications in biomedical and biotechnological fields.

Two types of biohybrids (with and without cholesterol) were developed starting with the chlorophyll-containing, artificial lipid bilayers prepared by hydration of a thin DPPC film. Chlorophyll *a* was successfully used as a spectral marker to obtain information at the molecular level in the artificial lipid bilayers. This enabled spectral monitoring of the bio-based composites by exploiting the fluorescence emission properties and strong visible absorption of the porphyrin macrocycle.

The procedure for obtaining these nanobioarchitectures is simple, efficient, economical (requiring small quantities of raw materials) and eco-friendly. It involves safe, self-assembly steps and ultrasound treatments in a bottom-up approach to build biocidal and antioxidant nanomaterials.

Cholesterol-containing biohybrids were shown to be more stable (ZP = −36.4 mV) and to be the most potent, free radical scavengers, possessing an antioxidant activity value of 73.25%. In addition, the cholesterol-containing, carbon-based biohybrids were the most potent antibacterial materials, offering inhibition zones of 12.4, 11.3 and 10.2 mm in diameter, against *Escherichia coli*, *Staphylococcus aureus* and *Enterococcus faecalis*, respectively. The antibacterial potential of these biohybrids can be exploited in nanotechological applications as antimicrobial coatings.

Based on the fluorescence analysis, we can conclude that the addition of small amounts of carbon nanotubes to liposome suspensions affected the structure and fluidity of the artificial lipid membranes. Chlorophyll *a* sensed the interaction between artificial lipid bilayers and SWCNTs. The cholesterol enhanced the anisotropy, inducing high order in the lipid membranes, and also decreased the mobility in the bilayers.

The bio-coating of CNTs with bio-inspired membranes may be an effective method of increasing the biocompatibility of the CNTs, giving rise to bionanocomposites with good physical stability, having both antioxidant and antimicrobial properties.

Acknowledgements

S. M. Iordache was supported by the strategic grant POSDRU/159/1.5/S/133652, “Integrated system to improve the quality of doctoral and postdoctoral research in Romania and promotion of the role of science in society” cofinanced by the European Social Fund within the Sectorial Operational Program Human Resources Development 2007–2013.

References

1. Sundberg, P.; Karppinen, M. *Beilstein J. Nanotechnol.* **2014,** *5,* 1104–1136. doi:10.3762/bjnano.5.123

2. Ruiz, A.; Suárez, M.; Martin, N.; Albericio, F.; Rodríguez, H. *Beilstein J. Nanotechnol.* **2014,** *5,* 374–379. doi:10.3762/bjnano.5.43
3. Ruiz-Hitzky, E.; Darder, M.; Aranda, P. An Introduction to Bio-nanohybrid Materials. In *Bio-inorganic Hybrid Nanomaterials: Strategies, Syntheses, Characterization and Applications;* Ruiz-Hitzky, E.; Ariga, K.; Lvov, Y. M., Eds.; Wiley-VCH: Weinheim, Germany, 2008; pp 1–40. doi:10.1002/9783527621446.ch1
4. Barbinta Patrascu, M. E.; Ungureanu, C.; Iordache, S. M.; Bunghez, I. R.; Badea, N.; Rau, I. *J. Mater. Chem. B* **2014,** *2,* 3221–3231. doi:10.1039/C4TB00262H
5. Barbinta-Patrascu, M. E.; Ungureanu, C.; Iordache, S. M.; Iordache, A. M.; Bunghez, I.-R.; Ghiurea, M.; Badea, N.; Fierascu, R.-C.; Stamatin, I. *Mater. Sci. Eng., C* **2014,** *39,* 177–185. doi:10.1016/j.msec.2014.02.038
6. Barbinta-Patrascu, M. E.; Bunghez, I.-R.; Iordache, S. M.; Badea, N.; Fierascu, R.-C.; Ion, R. M. *J. Nanosci. Nanotechnol.* **2013,** *13,* 2051–2060. doi:10.1166/jnn.2013.6857
7. Mashaghi, S.; Jadidi, T.; Koenderink, G.; Mashaghi, A. *Int. J. Mol. Sci.* **2013,** *14,* 4242–4282. doi:10.3390/ijms14024242
8. Rogers-Nieman, G. M.; Dinu, C. Z. *Wiley Interdiscip. Rev.: Nanomed. Nanobiotechnol.* **2014,** *6,* 327–337. doi:10.1002/wnan.1268
9. Guldi, D. M.; Martín, N. *Carbon Nanotubes and Related Structures. Synthesis, Characterization, Functionalization, and Applications;* Wiley-VCH: Weinheim, Germany, 2010.
10. He, H.; Pham-Huy, L. A.; Dramou, P.; Xiao, D.; Zuo, P.; Pham-Huy, C. *BioMed Res. Int.* **2013,** 578290. doi:10.1155/2013/578290
11. Firme, C. P., III; Bandaru, P. R. *Nanomedicine* **2010,** *6,* 245–256. doi:10.1016/j.nano.2009.07.003
12. Kam, N. W. S.; Jessop, T. C.; Wender, P. A.; Dai, H. *J. Am. Chem. Soc.* **2004,** *126,* 6850–6851. doi:10.1021/ja0486059
13. Villa, C. H.; Dao, T.; Ahearn, I.; Fehrenbacher, N.; Casey, E.; Rey, D. A.; Korontsvit, T.; Zakhaleva, V.; Batt, C. A.; Philips, M. R.; Scheinberg, D. A. *ACS Nano* **2011,** *5,* 5300–5311. doi:10.1021/nn200182x
14. Kolosnjaj-Tabi, J.; Szwarc, H.; Moussa, F. In vivo Toxicity Studies of Pristine Carbon Nanotubes: A Review. In *The Delivery of Nanoparticles;* Hashim, A. A., Ed.; InTech: Rijeka, Croatia, 2012; pp 37–58. doi:10.5772/34201
15. Yang, S.-T.; Luo, J.; Zhou, Q.; Wang, H. *Theranostics* **2012,** *2,* 271–282. doi:10.7150/thno.3618
16. Lim, J.-H.; Kim, S.-H.; Shin, I.-S.; Park, N.-H.; Moon, C.; Kang, S.-S.; Kim, S.-H.; Park, S.-C.; Kim, J.-C. *Birth Defects Res., Part B* **2011,** *92,* 69–76. doi:10.1002/bdrb.20283
17. Kolosnjaj-Tabi, J.; Hartman, K. B.; Boudjemaa, S.; Ananta, J. S.; Morgant, G.; Szwarc, H.; Wilson, L. J.; Moussa, F. *ACS Nano* **2010,** *4,* 1481–1492. doi:10.1021/nn901573w
18. Singh, G. P. B.; Baburao, C.; Pispati, V.; Pathipati, H.; Muthy, N.; Prassana, S. R. V.; Rathode, B. G. *Int. J. Res. Pharm. Chem.* **2012,** *2,* 523–532.
19. Bianco, A.; Kostarelos, K.; Partidos, C. D.; Prato, M. *Chem. Commun.* **2005,** 571–577. doi:10.1039/b410943k
20. Ghafari, P.; St-Denis, C. H.; Power, M. E.; Jin, X.; Tsou, V.; Mandal, H. S. *Nat. Nanotechnol.* **2008,** *3,* 347–351. doi:10.1038/nnano.2008.109
21. Kagan, V. E.; Konduru, N. V.; Feng, W.; Allen, B. L.; Conroy, J.; Volkov, Y.; Vlasova, I. I.; Belikova, N. A.; Yanamala, N.; Kapralov, A.; Tyurina, Y. Y.; Shi, J.; Kisin, E. R.; Murray, A. R.; Franks, J.; Stolz, D.; Gou, P.; Klein-Seetharaman, J.; Fadeel, B.; Star, A.; Shvedova, A. A. *Nat. Nanotechnol.* **2010,** *5,* 354–359. doi:10.1038/nnano.2010.44
22. New, R. R. C. *Liposomes: A practical approach;* IRL press: Oxford University, U.K., 1990.
23. Strain, H. H.; Svec, W. A. Extraction, separation, estimation, and isolation of the chlorophylls. In *The Chlorophylls;* Vernon, L. P.; Seely, G. R., Eds.; Academic Press: New York, NY, USA, 1966; pp 21–66.
24. Hsu, C.-Y.; Chao, P.-Y.; Hu, S.-P.; Yang, C.-M. *Food Nutr. Sci.* **2013,** *4,* 1–8. doi:10.4236/fns.2013.48A001
25. Lanfer-Marquez, U. M.; Barros, R. M. C.; Sinnecker, P. *Food Res. Int.* **2005,** *38,* 885–891. doi:10.1016/j.foodres.2005.02.012
26. Lakowicz, J. R. *Topics in Fluorescence Spectroscopy;* Kluwer Academic Publishers: New York, NY, USA, 2002.
27. Merényi, G.; Lind, J.; Eriksen, T. E. *J. Biolumin. Chemilumin.* **1990,** *5,* 53–56. doi:10.1002/bio.1170050111
28. Lind, J.; Merenyi, G.; Eriksen, T. E. *J. Am. Chem. Soc.* **1983,** *105,* 7655–7661. doi:10.1021/ja00364a032
29. Lacatusu, I.; Badea, N.; Oprea, O.; Bojin, D.; Meghea, A. *J. Nanopart. Res.* **2012,** *14,* 902–917. doi:10.1007/s11051-012-0902-9
30. Akhtar, S.; Sarker, M. R.; Hossain, A. *Crit. Rev. Microbiol.* **2014,** *40,* 348–359. doi:10.3109/1040841X.2012.742036
31. Toval, F.; Köhler, C.-D.; Vogel, U.; Wagenlehner, F.; Mellmann, A.; Fruth, A.; Schmidt, M. A.; Karch, H.; Bielaszewska, M.; Dobrindt, U. *J. Clin. Microbiol.* **2014,** *52,* 407–418. doi:10.1128/JCM.02069-13
32. Megged, O. *Pediatr. Nephrol.* **2014,** *29,* 269–272. doi:10.1007/s00467-013-2655-9
33. Zipfel, P. F.; Skerka, C. *Int. J. Med. Microbiol.* **2014,** *304,* 188–194. doi:10.1016/j.ijmm.2013.11.004
34. Horsley, H.; Malone-Lee, J.; Holland, D.; Tuz, M.; Hibbert, A.; Kelsey, M.; Kupelian, A.; Rohn, J. L. *PLoS One* **2013,** *8,* 1–13. doi:10.1371/journal.pone.0083637
35. Siddiqui, S. H.; Awan, K. H.; Javed, F. *Photodiagn. Photodyn. Ther.* **2013,** *10,* 632–643. doi:10.1016/j.pdpdt.2013.07.006
36. Ansari, M. A.; Khan, H. M.; Khan, A. A.; Malik, A.; Sultan, A.; Shahid, M.; Shujatullah, F.; Azam, A. *Biol. Med.* **2011,** *3,* 141–146.
37. Jorgensen, J. H.; Turnidge, J. D. Susceptibility test methods: dilution and disk diffusion methods. In *Manual of clinical microbiology,* 9th ed.; Murray, P. R.; Baron, E. J.; Jorgensen, J. H.; Landry, M. L.; Pfaller, M. A., Eds.; ASM Press: Washington, DC, USA, 2007; pp 1152–1172.
38. Liu, Y.-S.; Wen, C.-F.; Yang, Y.-M. *Sci. Adv. Mater.* **2014,** *6,* 954–962. doi:10.1166/sam.2014.1859
39. Mishra, P. R.; Al Shaal, L.; Müller, R. H.; Keck, C. M. *Int. J. Pharm.* **2009,** *371,* 182–189.
40. Jacobs, C.; Müller, R. H. *Pharm. Res.* **2002,** *19,* 189–194. doi:10.1023/A:1014276917363
41. Shameli, K.; Bin Ahmad, M.; Jazayeri, S. D.; Shabanzadeh, P.; Jahangirian, H.; Mahdavi, M.; Abdullahi, Y. *Int. J. Mol. Sci.* **2012,** *13,* 6639–6650. doi:10.3390/ijms13066639
42. Galano, A. *Nanoscale* **2010,** *2,* 373–380. doi:10.1039/b9nr00364a
43. Galano, A. *J. Phys. Chem. C* **2008,** *112,* 8922–8927. doi:10.1021/jp801379g
44. Fenoglio, I.; Tomatis, M.; Lison, D.; Muller, J.; Fonseca, A.; Nagy, J. B.; Fubini, B. *Free Radical Biol. Med.* **2006,** *40,* 1227–1233. doi:10.1016/j.freeradbiomed.2005.11.010
45. Watts, P. C. P.; Fearon, P. K.; Hsu, W. K.; Billingham, N. C.; Kroto, H. W.; Walton, D. R. M. *J. Mater. Chem.* **2003,** *13,* 491–495. doi:10.1039/b211328g
46. Barbinta Patrascu, M. E.; Cojocariu, A.; Tugulea, L.; Badea, N. M.; Lacatusu, I.; Meghea, A. *J. Optoelectron. Adv. Mater.* **2011,** *13,* 1153–1158.

47. Dong, X.; Tang, Y.; Lilly, M.; Aferchich, K.; Yang, L. *Nano LIFE* **2012,** *2,* 1230012–1230027. doi:10.1142/S1793984412300129
48. Simmons, T. J.; Lee, S.-H.; Park, T.-J.; Hashim, D. P.; Ajayan, P. M.; Linhardt, R. J. *Carbon* **2009,** *47,* 1561–1564. doi:10.1016/j.carbon.2009.02.005
49. Kang, S.; Pinault, M.; Pfefferle, L. D.; Elimelech, M. *Langmuir* **2007,** *23,* 8670–8673. doi:10.1021/la701067r

BEILSTEIN JOURNAL OF NANOTECHNOLOGY

Oxygen-plasma-modified biomimetic nanofibrous scaffolds for enhanced compatibility of cardiovascular implants

Anna Maria Pappa[1], Varvara Karagkiozaki[*1], Silke Krol[2], Spyros Kassavetis[3], Dimitris Konstantinou[1], Charalampos Pitsalidis[1], Lazaros Tzounis[1], Nikos Pliatsikas[3] and Stergios Logothetidis[1]

Full Research Paper

Open Access

Address:
[1]1Nanomedicine Group, Department of Physics, Lab for "Thin Films Nanosystems & Nanometrology" Aristotle University of Thessaloniki, 54124 Thessaloniki, Greece, [2]Fondazione IRCCS Neurologic Institute "Carlo Besta", IFOM-IEO-campus, Italy and [3]Department of Applied Physics, Aristotle University of Thessaloniki, 54124 Thessaloniki, Greece

Email:
Varvara Karagkiozaki[*] - vakaragk@physics.auth.gr

* Corresponding author

Keywords:
cardiovascular implants; electrospun nanofibers; plasma treatment; scaffold; tissue engineering

Beilstein J. Nanotechnol. **2015,** *6,* 254–262.
doi:10.3762/bjnano.6.24

Received: 01 September 2014
Accepted: 16 December 2014
Published: 22 January 2015

This article is part of the Thematic Series "Converging technologies for nanobio-applications".

Guest Editor: W. Lojkowski

Abstract

Electrospun nanofibrous scaffolds have been extensively used in several biomedical applications for tissue engineering due to their morphological resemblance to the extracellular matrix (ECM). Especially, there is a need for the cardiovascular implants to exhibit a nanostructured surface that mimics the native endothelium in order to promote endothelialization and to reduce the complications of thrombosis and implant failure. Thus, we herein fabricated poly-ε-caprolactone (PCL) electrospun nanofibrous scaffolds, to serve as coatings for cardiovascular implants and guide tissue regeneration. Oxygen plasma treatment was applied in order to modify the surface chemistry of the scaffold and its effect on cell attachment and growth was evaluated. The conditions of the surface modification were properly adjusted in order to define those conditions of the treatment that result in surfaces favorable for cell growth, while maintaining morphological integrity and mechanical behavior. Goniometry (contact angle measurements), scanning electron microscopy (SEM), atomic force microscopy (AFM), and X-ray photoelectron spectroscopy (XPS) measurements were used to evaluate the morphological and chemical changes induced by the plasma treatment. Moreover, depth-sensing nanoindentation was performed to study the resistance of the plasma-treated scaffolds to plastic deformation. Lastly, the cell studies indicated that all scaffolds were cytocompatible, with the plasma-treated ones expressing a more pronounced cell viability and adhesion. All the above findings demonstrate the great potential of these biomimetic tissue-engineering constructs as efficient coatings for enhanced compatibility of cardiovascular implants.

Introduction

Cardiovascular diseases represent one of the major causes of mortality in developing countries. For certain clinical cardiovascular applications, implanted devices need to be carefully designed in order to address all the drawbacks related to thrombosis and implant failure [1,2]. To achieve long-term results comparable to those of natural tissues, the ideal material should degrade and remodel with autologous cells into a natural structure [3] while the surface should be able to guide the process of tissue formation. To this end, biomimetic surface coatings and modifications using appropriate durable and biocompatible nanomaterials have already been applied [4-7]. To date, various sophisticated tissue-engineering structures that mimic the extracellular matrix (ECM) have been proposed, which aim to induce the highly desirable in situ endothelialization of vascular biomaterials while minimizing thrombogenicity and inflammation [8-10]. In the case of cardiovascular implants, though, the successful revascularization after implantation remains an unmet clinical problem [11]. This implies that endothelial cells must properly attach and migrate into the surface of the implanted material in order to form an appropriate network that will enable the delivery of blood and nutrients [12,13]. Therefore, the major challenge towards the long-term success of implants, is to find an appropriate surface coating that maintains the intricate balance between promoting in situ endothelialization, while inhibiting thrombosis and other systemic post-surgical complications [14].

Over the last decade, progress in the fundamental research of electrospun nanofibrous scaffolds has accelerated, with a special focus on biomedical applications [15]. This is due to their intrinsic similarities with the ECM of many tissues in the body, which renders them a powerful tool to control cell affinity and adhesion. Moreover, their high surface area to volume ratio, porosity and biodegradability favor cellular interactions, making them ideal candidates for polymer scaffolds [16]. As it is well known, the ideal scaffold should possess good bulk properties in terms of physical and mechanical stability, while the surface should provide high affinity with cells. In order to combine both prerequisites in one biomaterial, a common approach is to use synthetic biomaterials with adequate bulk properties and improve the surface functionalities by applying surface modification treatments [17]. Similarly, polycaprolactone (PCL) represents a commonly used biodegradable synthetic polymer for the fabrication of electrospun nanofibrous scaffolds [18], because of its beneficial bulk properties but lacks the proper surface environment for cellular attachment, mainly due to its strongly hydrophobic character [19]. To date, several surface-engineering techniques have been applied in order to chemically modify surfaces of electrospun nanofibers [9,20-22], including treatments by flame, corona discharge, plasma, photons, electron beam, ion beam, X-rays, and gamma rays. Among them, modifications based on plasma treatment have emerged as a very simple and promising approach to induce surface alterations or even introduce the desired chemical groups onto the surface of a material without affecting its bulk properties [22,23].

The aim of the present study was to effectively modify the surface of nanofibrous PCL scaffolds in order to promote ex situ endothelialization and potentially serve as coatings to enhance the compatibility of cardiovascular implants. The surface of the PCL nanofibrous scaffolds was modified through an oxygen (O_2)-plasma treatment, in order to increase their surface hydrophilicity by forming oxygen-containing groups at the surface and thus to improve cell adhesion and proliferation. The conditions of the plasma modification were properly adjusted in order to induce the desirable chemical surface changes while maintaining surface integrity and morphology. The applied power of the plasma was selected with respect to its effect on the structural and chemical composition of the scaffold. The untreated and plasma-treated nanofibrous scaffolds were evaluated in terms of surface topography, hydrophilicity, and surface chemistry in order to find the conditions that may lead to improved surface properties without affecting the morphology or the mechanical behaviour of the system. In depth nanoindentation measurements were conducted for the scaffolds under optimal conditions to assess the mechanical performance. MTT assay along with imaging techniques were used to evaluate the influence of the plasma treatment on cell attachment, morphology and viability.

Results and Discussion

Morphological characterization of the plasma-treated scaffolds

Electrospinning is a versatile and well-established technique broadly applied for the fabrication of nanofibrous meshes as scaffolds for tissue engineering applications. Electrospun scaffolds exhibit a preferential and easy to modulate morphology due to their unique geometrical features which replicate many in vivo structures [24,25]. The PCL nanofibrous scaffolds, prepared herein through electrospinning, were modified through a treatment with O_2-plasma using different plasma powers (P) of 20 W and 40 W, in order to render their surface more hydrophilic and thus the scaffold more biocompatible. Specifically, the treatment time was kept constant at 5 min, as prolonged time periods of plasma treatment has been already reported to negatively affect the morphology and integrity of the treated systems [26]. A morphological and surface characterization of the treated systems was performed in order to eval-

uate the optimum treatment conditions and the results are presented below.

The SEM micrographs of the untreated and the plasma-treated electrospun scaffolds are shown in Figure 1a–c. The images clearly indicate the effect of the plasma modification on the structural and surface integrity of the electrospun scaffolds. The unmodified fabricated nanofibers appeared interconnected and randomly stacked in a layer-by-layer configuration, forming pores between the fibers in the non-woven mesh network. It can be observed that the surface of the untreated and the surface-modified nanofibrous scaffolds after applying 20 W power was quite smooth and no morphologically significant differences were found. On the contrary, by increasing the power to 40 W, the plasma effect was very prominent and dramatically affected the morphology of the scaffolds, which resulted in a melting of the fibers as shown in Figure 1c. The mild treatment conditions (high magnification of image in Figure 1b) resulted in the melting of the thinner fibers of the scaffold, which is favorable for the cells, as it provides more space (micropores) between the fibers to elongate and spread [21]. This is highly preferable for certain cell types which exhibit the tendency to spread out and form an elongated cell body, such as the fibroblasts [26], which were incorporated in our study (mouse fibroblast cells-L929).

AFM has been a widely used technique for the observation of composite surfaces on the atomic scale. Plasma-treated surfaces have been effectively studied via AFM due to the ease of sample preparation and excellent resolution [27]. AFM was used in order to determine the topographical features of the studied surfaces and the effect of the plasma treatment on their roughness. The surface roughness parameters of the untreated and plasma-treated electrospun scaffolds are summarized in Table 1, while the obtained topographies of the samples are presented in Figure 1d–f. The average surface roughness (R_a), was found to increase after the O_2-plasma treatment with mild power conditions (P = 20 W) which is attributed to the incorporation of the polar groups on the surface. Indeed, during plasma treatment the polymer chains on the surface break and polar

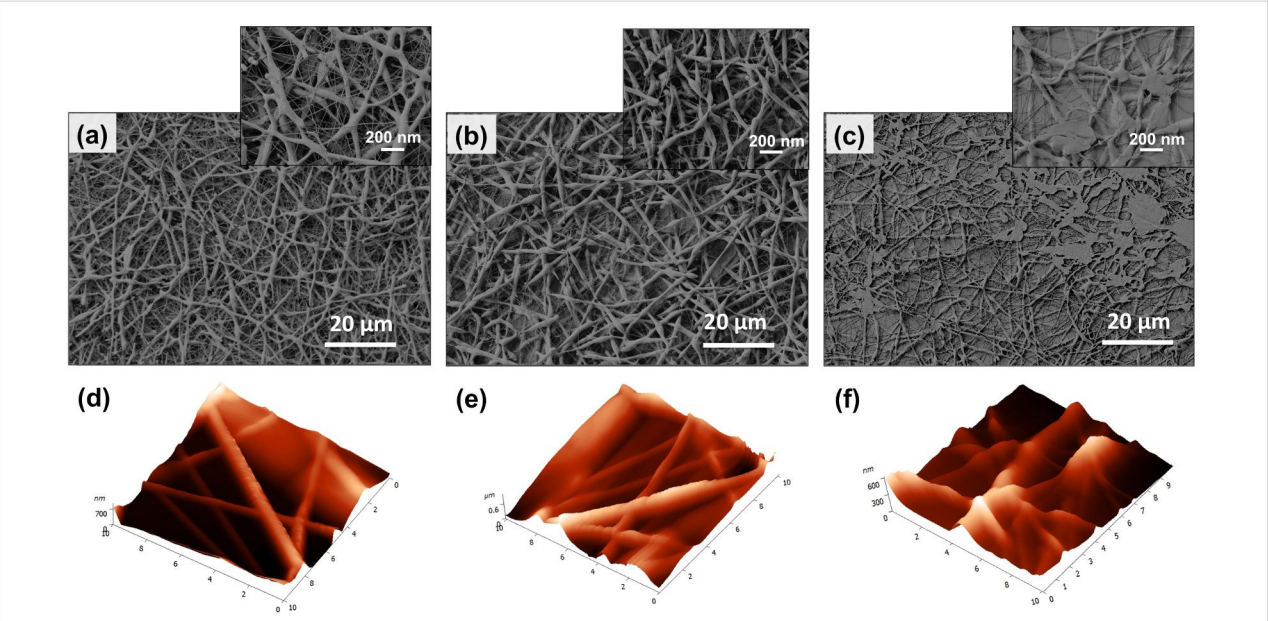

Figure 1: SEM and AFM images of the (a,d) untreated PCL electrospun scaffolds and of the O_2-plasma modified ones, with (b,e) P = 20 W and (c,f) P = 40 W (the axis in AFM images is in µm).

Table 1: Surface characteristics from AFM analysis and water contact angle measurements for the untreated and the O_2-plasma-treated nanofibrous scaffolds.

PCL scaffold	roughness, R_a (nm)	peak-to-valley, R_y (nm)	contact angle (degrees)
untreated	200.48	225.59	91.3
O_2, 20 W	245.25	287.22	21.4
O_2, 40 W	89.5	118.73	19.8

functional groups are created. This leads to an increase in the polarity and the surface energy, resulting in a roughened topography. Higher plasma power (P = 40 W) significantly decreased R_a resulting into smoother nanofibrous surfaces compared to the untreated samples, due to the partial polymer melting. These findings, which are in correlation with the morphological changes observed by SEM and AFM imaging, underline the positive effect of the mild power plasma conditions on the nanofibrous scaffolds in terms of surface topography.

Chemical characterization of the plasma-treated scaffolds

As can be observed from the contact angle measurements presented in Table 1, the untreated PCL scaffold demonstrated a water contact angle of 91.3°. A significant decrease of the contact angle was found for both modified systems with insignificant differences in the measured values (21.4° and 19.8° for P = 20 W and P = 40 W, respectively). The insignificant difference in the surface hydrophilicity of the two modified systems, indicates that O_2-plasma treatment alters the surface hydrophilicity even when applying relatively mild plasma conditions whereas the increase in the power of the plasma treatment does not appear to have any additional effect as far as the goniometry analysis is concerned. It is worth noting that the presented data from the contact angle measurements are particularly valid only for comparative purposes as the nanofibrous scaffolds are not smooth and homogeneous solid surfaces but highly porous structures. Thus, in our case, contact angle measurements are not a reliable technique to gain results concerning the wettability and the surface energy of each system independently [28].

In order to determine the chemical composition of the O_2-plasma-treated samples as well as the chemical alterations induced after the treatment, XPS measurements were performed. Specifically, high-resolution peak analysis of carbon 1s (C 1s) at the surface was performed for both untreated and plasma-treated PCL scaffolds. According to the obtained XPS data of the C 1s spectra in all the groups of samples three components can be observed, which correspond to the aliphatic carbon bonds (–C–C– or –C–H), carbon single bonded to oxygen (–C–OH or –C–O–), and carbonyl functional groups (O–C=O) located at approximately 285.0, 286.5, and 288.9 eV, respectively.

O_2-plasma treatment is a commonly used surface modification approach, to introduce oxygen-containing groups onto the surface of a polymer. This leads to an increase in the surface energy of the treated material and therefore enhances its hydrophilic behavior. During this process, the chemical alterations that are induced as a result of the radical reactions between the chain backbone of the polymer and the oxygen in the plasma, modify the surface chemistry, which results in higher numbers of oxygen-containing functional groups. Indeed, changes were observed by the XPS analysis in the intensity of the peaks of the untreated and plasma-treated electrospun PCL scaffolds (Figure 2). This provides evidence of the successful chemical alterations induced by the plasma treatment. These modifications include new oxygen-containing groups formed at the polymer surface, which are evident by the increase in the peak related to the carbonyl functional groups (–C=O). These groups contribute to the improvement of the surface hydrophilicity, which was also confirmed by the goniometry measurements [29]. In Table 2, all the data obtained from the XPS measurements are summarized by means of the surface atomic composition (%) as well as the concentration (%) for the different chemical bonds at the untreated as well as the treated surfaces. Notably, a significant deterioration of the chemical structure was observed in the case of increased plasma power treatment, in which a complete alteration of the C 1s core level peaks is observed. This effect can be presumably attributed to the extensive polymer melting induced by the high power plasma treatment. The significant degradation of the

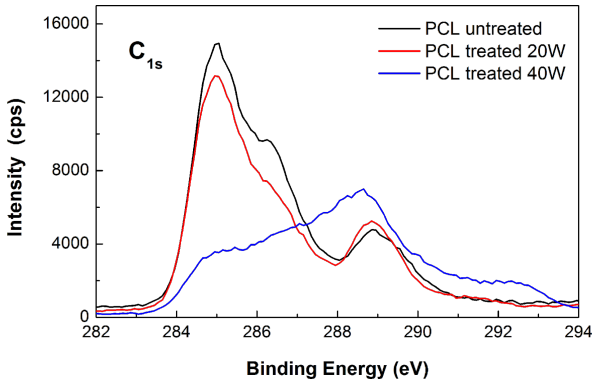

Figure 2: XPS spectra of the untreated PCL electrospun scaffolds and the O_2-plasma modified ones, with P = 20 W and P = 40 W.

Table 2: Surface atomic composition (atom %) and concentration of the different chemical bonds (%) on the untreated and the O_2-plasma-treated nanofibrous scaffolds.

%	untreated	O_2, 20 W	O_2, 40 W
C 1s	70.89	69.97	69.91
O 1s	29.11	30.03	30.29
C–C (285.0 eV)	44.2	44.8	13.0
C–O (286.5 eV)	35.0	33.8	22.2
C=O (288.9 eV)	20.8	21.4	48.5

chemical structure of the polymer in line with the deteriorated morphological and topographical characteristics observed through SEM and AFM imaging underline that the milder O_2-plasma treatment conditions are the most appropriate for enhancing the surface functionality without affecting the morphological properties and chemical structure of the polymer.

Mechanical behavior of the plasma-treated scaffolds

A basic principle in regenerative medicine is to maintain the structural integrity of a scaffold after implantation and also to provide the appropriate microstress environment to the cells. It is well known in the implants industry that the mechanical properties of implants should be adequate in order to sustain the stresses and to prevent premature failure [30]. Thus, it is of paramount importance that the coatings developed for implants exhibit a good mechanical performance, which matches with that of the native surrounding tissues. Plasma treatment is known to induce changes onto the outermost layer of a material without interfering with its bulk properties [23]. In order to further confirm this assumption nanomechanical measurements were conducted, in both mildly treated and untreated systems, and the obtained results were compared.

The effect of the O_2-plasma treatment on the mechanical properties of the PCL scaffold was studied by using dynamic nanoindentation. In Figure 3, the elastic modulus (E) values of the untreated and the O_2-plasma-treated PCL versus the contact depth are presented. In every nanoindentation test the same behavior was noticed: As the nanoindenter penetrates from the surface to the 'body' of the PCL films the E value decreases mainly due to the surface roughness of the PCL, and reaches a plateau after about 50 nm, which corresponds to the E of the sample. Therefore, the calculated E value, for the untreated and the O_2-plasma-treated PCL varies between 1–4 GPa and 1.5–2.5 GPa, respectively. Conclusively, the nanoindentation testing showed that the O_2-plasma did not degrade the mechanical properties of the PCL, in contrary the nanomechanical behavior of the PCL appears to be more homogeneous after the treatment, possibly due to the alternation/homogenization of the PCL surface properties.

Cellular performance of the plasma-treated scaffolds

As previously mentioned, the main advantage of the electrospun nanofibrous structures in tissue engineering is their morphological resemblance to the ECM, providing the appropriate microenvironment for the cells. Apart from the topographical features, biochemical features are also important to control and favor cell activity. Thus, the ultimate aim of the present work was to modify the hydrophobic surface of electrospun nanofibrous PCL scaffolds, in order to improve the surface chemistry and favor the cell-material interactions without dramatically affecting the morphological features of the material, nor its physicochemical structure. In order to validate the effect of the surface modification on the cell behavior, MTT biological assay in line with imaging techniques were conducted in order to observe the cells viability as well as their morphology and attachment onto the nanofibrous scaffolds.

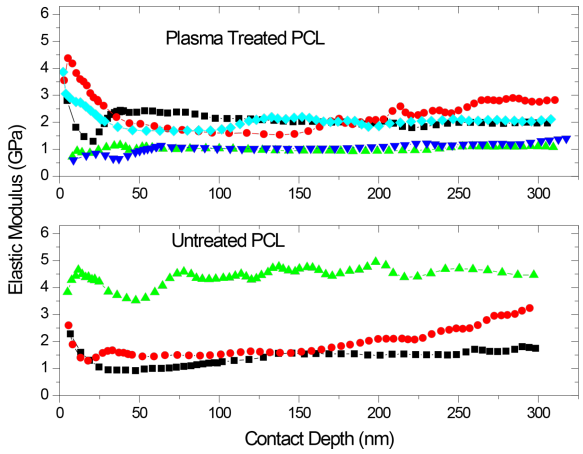

Figure 3: The elastic modulus values of the untreated PCL electrospun scaffolds and the plasma-modified ones (20 W) versus the contact depth. Every curve comes from a nanoindentation measurement to a different surface location of the samples.

Cell viability assay

MTT cell viability assay was performed to the unmodified along with the plasma-treated (P = 20 W) scaffold, in order to evaluate the effect of the surface modification on the cellular performance of the fabricated samples in terms of cell viability. The cells used in the present reference study were mouse fibroblasts (L929). In Figure 4a and Figure 4b, the MTT results of the cytotoxicity levels of all the samples (i.e., control group, aluminum foil, untreated scaffold and mildly treated scaffold) in direct contact with the L929s are given. According to the findings, all the fabricated systems were found to be cytocompatible after a period of seven days and exhibited cell viability levels similar to those of the control group. An enhancement in the cell viability (ca. 10%) can be observed in the case of the treated PCL scaffolds after seven days. The improved cellular performance can be attributed to the effective chemical and topographical alterations induced by the plasma treatment, in terms of the increased hydrophilicity as well as surface roughness, respectively. It is noteworthy that in all groups of samples, a general trend in the cell viability, a decrease after three days of culture and an increase afterwards, was observed. This can be attributed to the number of cells that finally managed to adhere onto the desired surfaces, given the fact that cells need time to

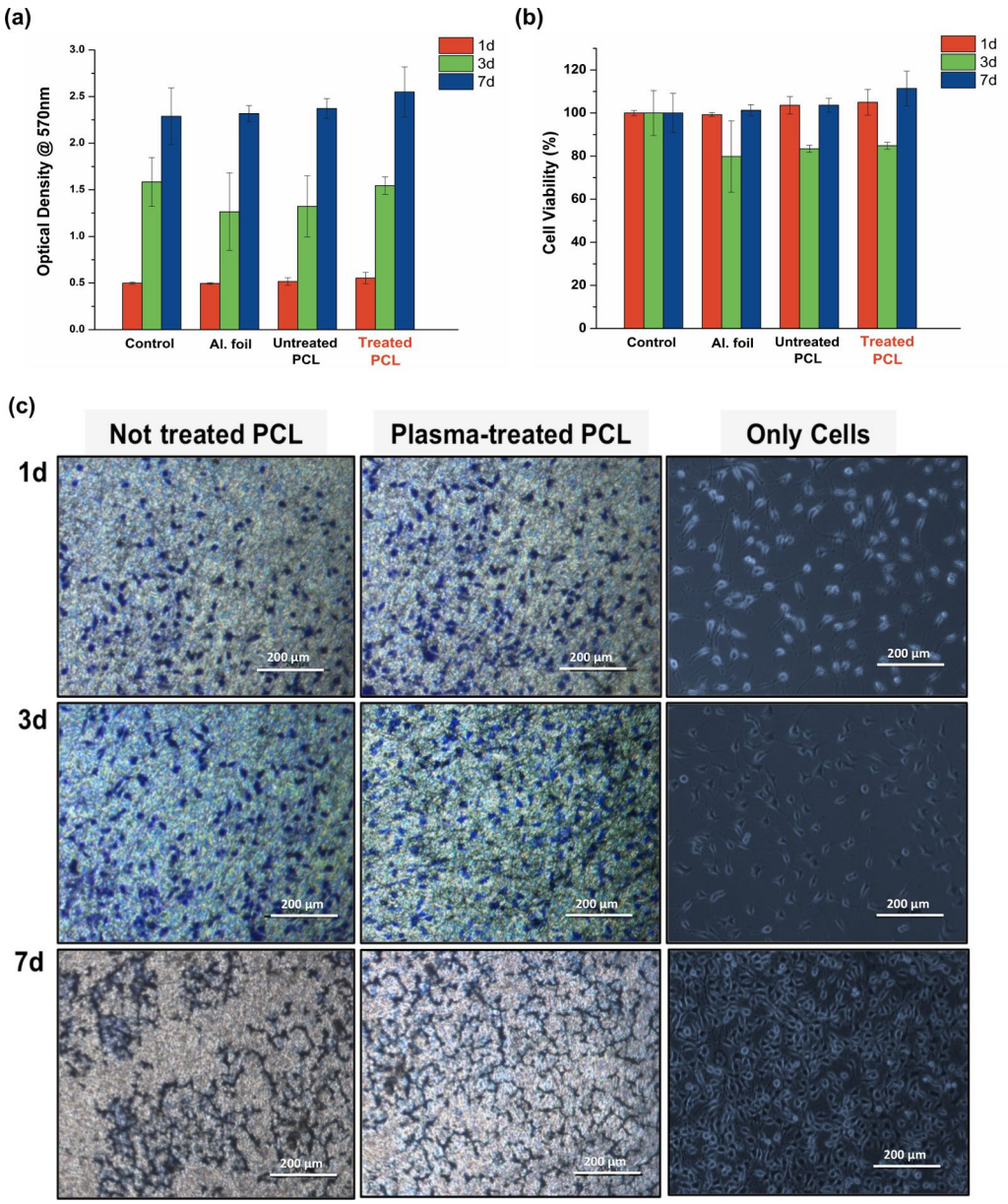

Figure 4: (a,b) MTT assay of L929 cells in direct contact with the examined systems after 1, 3 and 7 days, in terms of optical density values as well as the normalized % cell viability, respectively, and (c) optical imaging of the cell morphology in the predetermined time periods for the untreated and the plasma treated scaffolds.

adapt in new conditions (lag phase). The increase in the cell viability after the three days, which is more apparent in the case of the treated samples indicates the growth and proliferation of the cells in their new microenvironment.

Cell adhesion and proliferation

According to Figure 4c, fibroblasts seemed to be securely attached and spread on the surface, regardless of the surface treatments. Interestingly, cells seemed to be attached and spread more on the plasma-treated scaffold surfaces compared to the untreated surfaces, during the first day. A notable enhancement of the spreading is observed in the following days, with higher cell confluency and proliferation in the treated scaffolds compared with the unmodified ones. After seven days of culture, the cells seem to have obtained a spindle-like morphology and especially in the case of the treated scaffolds a notably more uniform spatial distribution of the cells is observed.

The morphological analysis through SEM imaging, of the direct contact assay with the L929 fibroblasts for the periods of 1, 3 and 7 days for the untreated and the plasma treated samples is presented in Figure 5. Particularly, a typical spindle- shape cell

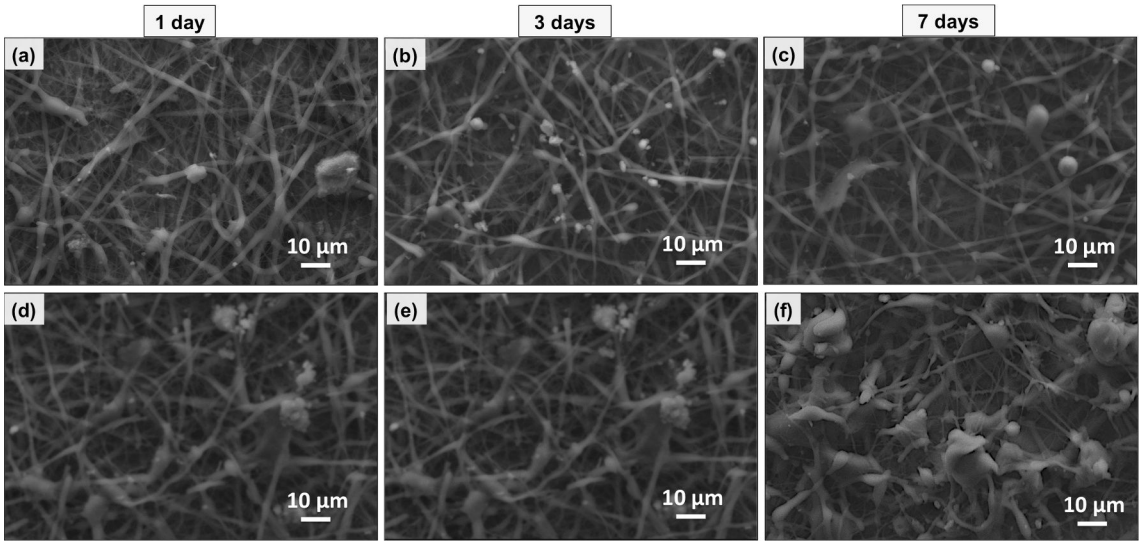

Figure 5: SEM micrographs of the (a–c) untreated PCL electrospun scaffolds for 1,3 and 7 days of direct contact with cells and (d–f) and of the O_2-plasma-modified scaffolds, at the predetermined time periods.

morphology is observed in the treated samples, while in the untreated surfaces the cells seem to have maintained their round shape. Moreover, the cells seem to be well-dispersed and tightly packed after 7 days in the modified surfaces. The amount of cells is evidently higher in the modified surfaces, underlying the higher affinity of cells the treated surfaces exhibit. After 7 days, a flattened morphology of cells is clearly observed, covering partially the plasma-treated surface. The enhanced cell adhesion and proliferation observed in the modified systems is attributed to plasma-induced chemical alterations of the surface and is in line with the results obtained from the physicochemical characterization of the systems. All the above findings strongly indicate the positive influence of the plasma treatment over the cell adhesion and proliferation.

Conclusion

Plasma-assisted treatment of the surface of biomaterials has proven to be a straightforward and versatile method for modifying the chemical composition of the surface without affecting its bulk properties. Overall, PCL nanofibrous scaffolds with morphological features that mimic the ECM, and adequate porosity as well as surface hydrophilicity, were successfully fabricated by the electrospinning method. In order to make the scaffold more cytocompatible, oxygen-plasma treatment was used to modify the surface chemistry along with its nanotopography without causing any deterioration of the structure or the integrity of the scaffold and without affecting its mechanical and physical bulk properties. This approach, of controlling the surface properties along with the topographical nanoscale features of the scaffolds could be very useful in the design of novel biomimetic coatings, able to guide tissue regeneration especially in cardiovascular implant industry, where in situ vascular regeneration remains an unmet challenge.

Experimental

Scaffold design and fabrication

Materials and methods

Polycaprolactone (PCL), M_n = 45,000 Da, chloroform (≥99.8%), methanol (≥99.9%) were obtained from Sigma (Sigma-Aldrich, Greece). All reagents were used without further purification and all solutions were prepared by deionised water.

The nanofibrous scaffolds were fabricated by electrospinning through the electrostatic spray deposition (ESD) method, (Esprayer ES-2000S, Fuence, Japan) onto aluminum foil and glass substrates. For the fabrication of the polymeric solutions, a solution of PCL was prepared with a total concentration of 20–25 wt % in a solvent mixture of chloroform: methanol (3:1). The solution was electrospun from a 5 mL syringe with a 24 gauge needle and mass flow rate of 10–15 µL/min. A high voltage (15–20 kV) was applied to the tip of the needle when the fluid jet was ejected. The distance between the needle and the moving collector in the XY stage, was set at 40 mm. The glass substrates were cleaned prior to electrospinning with isopropanol and methanol and blow-dried using N_2 flow. Each fabricated film was left overnight to allow the evaporation of any residual solvents.

Plasma treatment

After the fabrication of the electrospun scaffolds, plasma treatment on the nanofibrous scaffolds was performed. The treat-

ment was carried out on a low frequency (40 kHz, 0–200 W) plasma generator (ATTO, Diener Electronic) while using oxygen gas. The procedure was undertaken in a vacuum chamber, which was first evacuated to less than 0.1 mTorr. By supplying oxygen to the chamber the pressure was maintained to 0.25 mTorr while the power was adjusted to up to 40 W for 5 min. Finally, the treated samples were further exposed to the oxygen atmosphere for another 10 min before the sample was taken out from the chamber.

Characterization techniques

Morphological characterization

SEM: The morphological analysis of the PCL scaffolds was carried out by using scanning electron microscopy (SEM, NEON40, Carl Zeiss). In order to visualize and evaluate the morphological characteristics of the investigated materials, secondary electron detector was used.

AFM: Atomic force microscopy, AFM (AFM Solver, NT-MDT) was used to determine surface topography and roughness of the plasma-treated samples.

Chemical characterization

Contact angle: Static contact angle measurements using water (Contact angle-surface tensionmeter CAM200, KSV Instruments Ltd) for the untreated and plasma-treated electrospun PCL scaffolds were performed to study and compare the effect of the two treatments on the surface hydrophilicity. At least six different measurements on the plasma-treated surfaces were obtained and the average values for contact angles were calculated. The maximum error in the contact angle measurement did not exceed ±3%.

XPS: X-ray photoelectron spectroscopy (XPS) analysis of the surface layers was carried out in an Axis Ultra DLD system by Kratos Analytical using a monochromated Al $K\alpha_1$ X-ray beam as the excitation source. The analyzed area had an elliptical shape with the two axes being about 400 and 700 μm. The pass energy was 160 eV for survey scans and 20 eV for HR spectra. In the latter case, the pass energy would result in a broadening (FWHM) of less than 500 meV for the Ag 3d line. Data interpretation was performed with the Kratos-Vision software.

Mechanical characterization

Nanoindentation: Dynamic nanoindentation testing (continuous stiffness measurements, Nanoindenter XP) was carried out. A Berkovich type diamond nanoindenter with nominal tip roundness of ca. 50 nm was used to test the samples. Several nanoindents were made to different surface locations of the samples to 300 nm maximum penetration depth. The nanoindentation load–displacement curves were analyzed by using the Oliver–Pharr model to calculate the elastic modulus of the samples versus the indenter penetration (contact) depth [31].

Cell studies

MTT assay: MTT assay (Sigma-Aldrich, Germany) was used to evaluate cell viability. The cells used in this study were mouse fibroblasts L929 and were kindly offered from the Department of Biochemistry of the Aristotle University of Thessaloniki. In a similar manner as described in [32], the cell growth was stopped after 1 day, 3 days and 1 week. After each time point, the cells were incubated with a tenth of the medium of the bromide in 5% CO_2 (37 °C, 2 h) to allow the formation of water-insoluble formazan crystals. The optical densities (O.D.) of the solutions were read with a spectrophotometer, at the wavelength of 570 nm with respect to the reference wavelength of 690 nm. Data (n = 3) were presented as means of O.D. values as well as normalized according to the control and presented as % cell viability.

Optical imaging through methylene blue staining: Once fibroblasts were seeded onto either unmodified or surface-modified nanofibrous scaffolds, cellular morphology and cell attachment were observed after 1, 3 and 7 days. Cells were fixed, after the predetermined time periods, in 4% formaldehyde/PBS, at rt for 20 min, permeabilized with PBS and incubated with methylene blue (blue fluorescence) at rt for 30 min. The cell surface was observed with an optical microscope (Carl Zeiss, Germany).

Acknowledgements

This study was partially supported by the NanoCardio Project "Nanomedicine for Advanced, Bioactive /-mimetic materials for Cardiovascular Implants", funded by GSRT Greece and European Commission. The authors would like to acknowledge Professor Theodora Choli-Papadopoulou and the Department of Biochemistry of the Aristotle University of Thessaloniki, for supplying us with the cells used in the present work.

References

1. de Valence, S.; Tille, J.-C.; Chaabane, C.; Gurny, R.; Bochaton-Piallat, M.-L.; Walpoth, B. H.; Möller, M. *Eur. J. Pharm. Biopharm.* **2013,** *85,* 78–86. doi:10.1016/j.ejpb.2013.06.012
2. Karagkiozaki, V. *J. Nanopart. Res.* **2013,** *15,* 1529. doi:10.1007/s11051-013-1529-1
3. Innocente, F.; Mandracchia, D.; Pektok, E.; Nottelet, B.; Tille, J.-C.; de Valence, S.; Faggian, G.; Mazzucco, A.; Kalangos, A.; Gurny, R.; Moeller, M.; Walpoth, B. H. *Circulation* **2009,** *120,* S37–45. doi:10.1161/CIRCULATIONAHA.109.848242
4. Schmehl, J. M.; Harder, C.; Wendel, H. P.; Claussen, C. D.; Tepe, G. *Cardiovasc. Revasc. Med.* **2008,** *9,* 255–262. doi:10.1016/j.carrev.2008.03.004

5. Karagkiozaki, V. C.; Logothetidis, S. D.; Kassavetis, S. N.; Giannoglou, G. D. *Int. J. Nanomed.* **2010,** *5,* 239–248. doi:10.2147/IJN.S7596
6. Karagkiozaki, V.; Vavoulidis, E.; Karagiannidis, P. G.; Gioti, M.; Fatouros, D. G.; Vizirianakis, I. S.; Logothetidis, S. *Int. J. Nanomed.* **2012,** *7,* 5327–5338. doi:10.2147/IJN.S31185
7. Karagkiozaki, V.; Logothetidis, S.; Laskarakis, A.; Giannoglou, G.; Lousinian, S. *Mater. Sci. Eng., B* **2008,** *152,* 16–21. doi:10.1016/j.mseb.2008.06.013
8. Janvikul, W.; Uppanan, P.; Thavornyutikarn, B.; Kosorn, W.; Kaewkong, P. *Procedia Eng.* **2013,** *59,* 158–165. doi:10.1016/j.proeng.2013.05.106
9. Yoo, H. S.; Kim, T. G.; Park, T. G. *Adv. Drug Delivery Rev.* **2009,** *61,* 1033–1042. doi:10.1016/j.addr.2009.07.007
10. Jo, S.; Kang, S. M.; Park, S. A.; Kim, W. D.; Kwak, J.; Lee, H. *Macromol. Biosci.* **2013,** *13,* 1389–1395. doi:10.1002/mabi.201300203
11. Karagkiozaki, V.; Logothetidis, S.; Vavoulidis, E. Nanomedicine Pillars and Monitoring Nano–biointeractions. In *Nanomedicine and Nanobiotechnology;* Logothetidis, S., Ed.; Springer: Berlin, Germany, 2012; pp 27–56. doi:10.1007/978-3-642-24181-9_2
12. Hung, H.-S.; Chen, H.-C.; Tsai, C.-H.; Lin, S.-Z. *Cell Transplant.* **2011,** *20,* 63–70. doi:10.3727/096368910X532864
13. Unger, R. E.; Peters, K.; Huang, Q.; Funk, A.; Paul, D.; Kirkpatrick, C. J. *Biomaterials* **2005,** *26,* 3461–3469. doi:10.1016/j.biomaterials.2004.09.047
14. de Mel, A.; Jell, G.; Stevens, M. M.; Seifalian, A. M. *Biomacromolecules* **2008,** *9,* 2969–2979. doi:10.1021/bm800681k
15. Ma, Z.; Kotaki, M.; Inai, R.; Ramakrishna, S. P. *Tissue Eng.* **2005,** *11,* 101–109. doi:10.1089/ten.2005.11.101
16. Cheng, Q.; Lee, B. L.-P.; Komvopoulos, K.; Yan, Z.; Li, S. *Tissue Eng., Part A* **2013,** *19,* 1188–1198. doi:10.1089/ten.tea.2011.0725
17. Yan, D.; Jones, J.; Yuan, X. Y.; Xu, X. H.; Sheng, J.; Lee, J. C.-M.; Ma, G. Q.; Yu, Q. S. *J. Biomed. Mater. Res., Part A* **2013,** *101,* 963–972. doi:10.1002/jbm.a.34398
18. Cipitria, A.; Skelton, A.; Dargaville, T. R.; Dalton, P. D.; Hutmacher, D. W. *J. Mater. Chem.* **2011,** *21,* 9419. doi:10.1039/C0JM04502K
19. Ma, Z.; Mao, Z.; Gao, C. *Colloids Surf., B* **2007,** *60,* 137–157. doi:10.1016/j.colsurfb.2007.06.019
20. Goddard, J. M.; Hotchkiss, J. H. *Prog. Polym. Sci.* **2007,** *32,* 698–725. doi:10.1016/j.progpolymsci.2007.04.002
21. Martins, A.; Pinho, E. D.; Faria, S.; Pashkuleva, I.; Marques, A. P.; Reis, R. L.; Neves, N. M. *Small* **2009,** *5,* 1195–1206. doi:10.1002/smll.200801648
22. Jacobs, T.; Morent, R.; De Geyter, N.; Dubruel, P.; Leys, C. *Plasma Chem. Plasma Process.* **2012,** *32,* 1039–1073. doi:10.1007/s11090-012-9394-8
23. Morent, R.; De Geyter, N.; Desmet, T.; Dubruel, P.; Leys, C. *Plasma Processes Polym.* **2011,** *8,* 171–190. doi:10.1002/ppap.201000153
24. Nandakumar, A.; Tahmasebi Birgani, Z.; Santos, D.; Mentink, A.; Auffermann, N.; van der Werf, K.; Bennink, M.; Moroni, L.; van Blitterswijk, C.; Habibovic, P. *Biofabrication* **2013,** *5,* 015006. doi:10.1088/1758-5082/5/1/015006
25. Chen, J.-P.; Su, C.-H. *Acta Biomater.* **2011,** *7,* 234–243. doi:10.1016/j.actbio.2010.08.015
26. Wan, Y.; Tu, C.; Yang, J.; Bei, J.; Wang, S. *Biomaterials* **2006,** *27,* 2699–2704. doi:10.1016/j.biomaterials.2005.12.007
27. Grythe, K. F.; Hansen, F. K. *Langmuir* **2006,** *22,* 6109–6124. doi:10.1021/la053471d
28. Wang, X. D.; Peng, X. F.; Lu, J. F.; Liu, T.; Wang, B. X. *Heat Transfer Res.* **2004,** *33,* 201–210. doi:10.1002/htj.20013
29. Lai, J.; Sunderland, B.; Xue, J.; Yan, S.; Zhao, W.; Folkard, M.; Michael, B. D.; Wang, Y. *Appl. Surf. Sci.* **2006,** *252,* 3375–3379. doi:10.1016/j.apsusc.2005.05.038
30. Pan, Z.; Ding, J. *Interface Focus* **2012,** *2,* 366–377. doi:10.1098/rsfs.2011.0123
31. Oliver, W. C.; Pharr, G. M. *J. Mater. Res.* **2011,** *7,* 1564–1583. doi:10.1557/JMR.1992.1564
32. Domingos, M.; Intranuovo, F.; Gloria, A.; Gristina, R.; Ambrosio, L.; Bártolo, P. J.; Favia, P. *Acta Biomater.* **2013,** *9,* 5997–6005. doi:10.1016/j.actbio.2012.12.031

License and Terms

The definitive version of this article is the electronic one which can be found at: doi:10.3762/bjnano.6.24

BEILSTEIN JOURNAL OF NANOTECHNOLOGY

Hollow plasmonic antennas for broadband SERS spectroscopy

Gabriele C. Messina, Mario Malerba, Pierfrancesco Zilio, Ermanno Miele, Michele Dipalo, Lorenzo Ferrara and Francesco De Angelis*

Full Research Paper

Open Access

Address:
Istituto Italiano di Tecnologia, Nanostructures Department, Via Morego 30, 16163 Genova, Italia

Email:
Francesco De Angelis* - francesco.deangelis@iit.it

* Corresponding author

Keywords:
biosensing; multiband field enhancement; plasmonics; Raman spectroscopy; SERS

Beilstein J. Nanotechnol. **2015,** *6,* 492–498.
doi:10.3762/bjnano.6.50

Received: 29 August 2014
Accepted: 22 January 2015
Published: 18 February 2015

This article is part of the Thematic Series "Converging technologies for nanobio-applications".

Guest Editor: W. Lojkowski

Abstract

The chemical environment of cells is an extremely complex and multifaceted system that includes many types of proteins, lipids, nucleic acids and various other components. With the final aim of studying these components in detail, we have developed multiband plasmonic antennas, which are suitable for highly sensitive surface enhanced Raman spectroscopy (SERS) and are activated by a wide range of excitation wavelengths. The three-dimensional hollow nanoantennas were produced on an optical resist by a secondary electron lithography approach, generated by fast ion-beam milling on the polymer and then covered with silver in order to obtain plasmonic functionalities. The optical properties of these structures have been studied through finite element analysis simulations that demonstrated the presence of broadband absorption and multiband enhancement due to the unusual geometry of the antennas. The enhancement was confirmed by SERS measurements, which showed a large enhancement of the vibrational features both in the case of resonant excitation and out-of-resonance excitation. Such characteristics indicate that these structures are potential candidates for plasmonic enhancers in multifunctional opto-electronic biosensors.

Introduction

Cells are extremely complex systems that consist of hundreds of different molecules that can react and give rise to many different chemical processes. In addition to the complexity of the cellular chemical environment, it must also be considered that some of the biomolecules of interest are present in very low concentrations. Therefore, monitoring such an environment requires techniques that can offer both flexibility and high sensitivity for all cases. In other words, the investigation of the biological functions of living cells requires the acquisition of information from many different cell parts. For example, considering the most common investigation method in biology, namely fluorescence spectroscopy, it offers very high sensi-

tivity, but at the cost of being sensitive only to those molecules for which the label has been applied to the bio-system. Most commonly, only a few selected components of the cells are stained and observed simultaneously by fluorescence microscopy: for example, membrane lipids together with the nucleus and cytoskeleton.

As an alternative to fluorescence methods, Raman spectroscopy is gaining attention as a technique for the study of live cells as it is a label-free non-invasive method and, moreover, it is not affected by photobleaching. Raman spectroscopy investigates the molecular bonds of all cell elements; therefore, it is potentially suitable for studying the entire cell environment without requiring the labelling of specific features of interest. However, the main drawback of Raman spectroscopy in this regard is the intrinsically low signal intensity, which leads to unsuitably high detection limits. In this respect, the exploitation of plasmonics for enhancing Raman signal has become an important factor for the routine application of this technique to biology.

There has been a significant increase in the number of studies concerning applications based on plasmonic effects in recent years. The areas of interest range from biomedicine, with examples of biosensing devices based on surface enhanced Raman scattering (SERS) enhancement [1-3], fluorescence [4,5], the surface plasmon resonance effect [6,7], mapping and imaging [8-10], to nanotechnology, with several works related to nanolithography [11,12], nanofocusing [13,14], nanolasers [15,16], waveguides [17,18] and magnetic field enhancement [19].

In these various disciplines, the rise of a trend targeting high performance spectroscopy techniques for biomolecules and cells can be recognized. Raman spectroscopy has already been implemented for whole live cell imaging [20] as well as its biological components [21].

It is well known that plasmons offer a great potential innovation in this regard because of their ability to capture and confine incident radiation in the so-called hotspots. To maximize this capability, plasmonic antennas can be designed to resonate at the desired excitation wavelength. As a consequence, they are efficient only in a limited spectral band around the tailored resonance wavelength, rather than being useful over the entire vis–NIR range, which is desirable for Raman spectroscopy of biological specimens.

On the other hand, the Raman spectroscopy fingerprint of cells includes over 1000 features [22] and many of them emit a much higher signal when excited at a specific wavelength. For this reason, there is the need for an enhancement method that allows for high enhancement values over a wide range of exciting wavelengths. With this, the same device can be exploited to perform highly sensitive SERS spectroscopy on all cell features using various excitation wavelengths. In a recent paper it was demonstrated that 3D hollow nanoantennas are capable of broadband absorption in the visible range of radiation [23].

In this work an experimental determination of the field enhancement supported by numerical calculations is presented. This shows how broadband absorption can be converted to multiband enhancement at the nanometer scale. This ability relies on the 3D nature of hollow vertically aligned (with respect to the metallic substrate plane) nanoantennas. The multiband behavior exhibited by these hollow nanoantennas may be a key factor for highly sensitive Raman measurements on the various components of the whole cell using an extended range of excitation light sources. Moreover, the 3D nature of these nanostructures allows them to be connected to electric power sources without disrupting the plasmon activity, thus opening their exploitation in the majority of the above cited fields.

Results and Discussion

Optimization of the electric field enhancement

The possibility of obtaining three-dimensional hollow nanoantennas with a high aspect ratio through an innovative technique based on secondary electron lithography was previously demonstrated [23]. Such a technique presents numerous advantages such as high versatility, allowing the production of structures with different sections, heights and diameters by controlling parameters such as the resist thickness and the beam energy. It is also conceivable to vary the angle of the ion milling, leading to the formation of tilted antennas. Moreover, the possibility of covering the polymer template with different materials expands the range of novel applications for such structures. In this paper, we exploit this fabrication approach to obtain cylindrical hollow antenna structures consisting of an inverted polymer covered with silver, as shown in Figure 1.

The inner cavity adds remarkable new functions (with respect to common cylindrical structures), namely: (i) efficient excitation of high order modes that results in an effective broadband absorption, (ii) the capability of concentrating the electric field in 3D hollow nanocavities, and (iii) the capability of connecting the plasmonic antennas to a metallic film (i.e., an electrode) without preventing their plasmonic function. In particular, the last point represents an important breakthrough, since it enables the combination of plasmonic with electrical functionalities: the antennas can be used also as nanoelectrodes for photovoltaic, electro-photochemical catalysis, optoelectronic and bio-electrochemical devices.

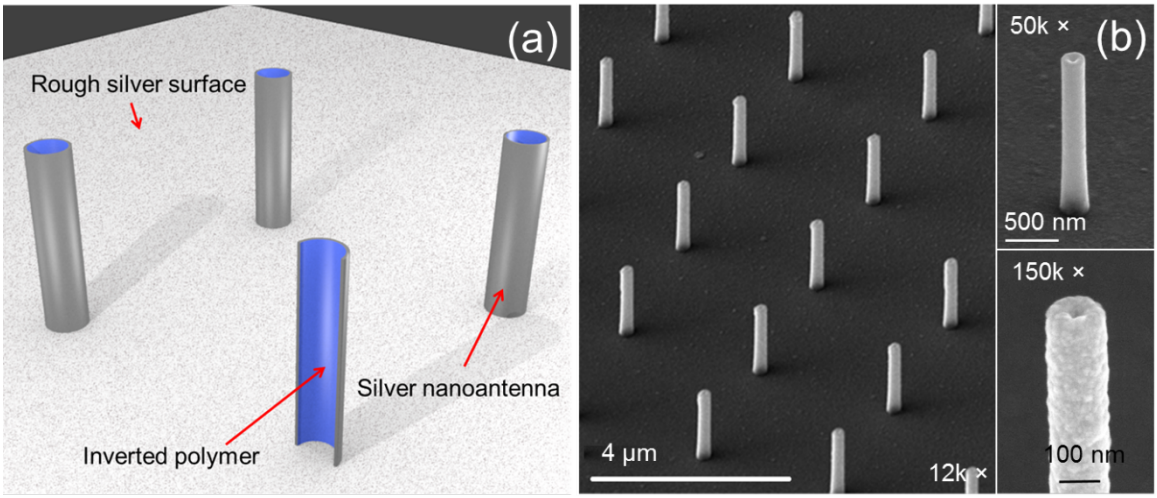

Figure 1: (a) Illustrative scheme representing the structure of a single antenna and (b) SEM images at different magnifications showing the array of antennas fabricated for this work.

As a final remark, it should also be considered that the proposed method is fast with respect to other approaches regarding the fabrication of the plasmonic nanostructures [24,25] including those based on FIB milling. In fact, it has been calculated that fabrication on the order of 100k structures per hour with fine spatial control and geometrical accuracy [23] can be accomplished, suggesting the possibility of covering large areas such as chips, printed circuit boards (PCBs) or multielectrode array (MEA) surfaces. To fully understand the potential of nanofabricated arrays, numerical calculations based on finite element method analysis aimed at modeling the behavior of hollow antennas have been performed.

The goal of the simulations was to maximize the enhancement of the electric field in the visible range (centered at around $\lambda = 630$ nm) in terms of both field amplitude and bandwidth.

We performed scattering simulations of a single antenna illuminated by TM polarized light impinging at 5° with respect to normal. The simulation layout realistically reproduced the fabricated structure, as depicted in Figure 1a. The scattered field is absorbed by perfectly matched layers placed all around the structure (not shown). As a figure of merit, we considered the electric field in air sampled 1 nm above the upper edge of the antenna.

In Figure 2, the values of field amplitude enhancement calculated for antennas whose height varies from 700 to 1800 and radius varies from 65 to 100 nm are shown. These parameter ranges have been chosen according to extended experiments and calculations (not reported for brevity). In order to save calculation time, we neglected the surface roughness in this optimization, whereas it will be considered later for the evaluation of the electric field enhancement. The model considers antennas with an 18 nm thick silver layer deposited on the surface. The field enhancement map shows several maxima as a function of the antenna height, which correspond to different orders of vertical Fabry–Perot resonances [23]. The calculations suggest that the maximum value of electromagnetic enhancement at around 630 nm excitation is 80 times the amplitude of the incoming electric field, and can be achieved for antennas of height $H = 1400$ nm and radius $R = 80$ nm.

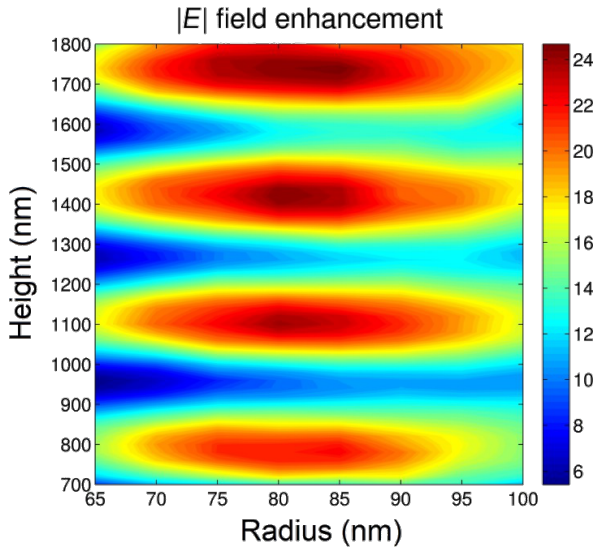

Figure 2: Electric field amplitude of silver antennas as a function of height and external radius. The maximum value of the field enhancement was found at an excitation wavelength of $\lambda = 630$ nm for $H = 1400$ and $R = 80$ nm.

Certainly, various geometries corresponding to different spectral bands of interest (both in terms of band position and width) are possible. Thus, by changing the device geometry, the optical response can be tuned according to specific needs. Therefore, the results presented here are considered to be representative of the general capabilities of this class of 3D devices. It is noted that the employment of antenna arrays could further tune and improve the optical response, especially in terms of absorption. However, here the properties of an isolated nanostructure are presented to better highlight its intrinsic features rather than those emerging from group properties.

For the geometry optimized in this work (1.4 µm height and 160 nm width), the metal absorption and the enhancement in the visible range for a single antenna with a surface roughness of 4 nm on the tip was calculated. The results are reported in Figure 3 with the limited spectral range of 400–900 nm shown for clarity. The device exhibits very good performance regarding both the electric field enhancement and absorption.

Both spectra are characterized by numerous peaks, partially overlapped in a quasi-continuous profile. The electric field enhancement exhibits a minimum value of 50 times up to maximum of 200 times at 630 nm, as was expected from the optimization. However, the absorption only varies from a value of 20% in the NIR up to about 50% at 630 nm. Even though a complete analysis of the spectral features is not the main goal of this work, it can be noted that there is no one-to-one correspondence between absorption and field enhancement peaks. This behavior can be related to the fact that the electromagnetic radiation can penetrate inside the hollow nanocavity, as demonstrated in our previous work [23], thus generating absorption peaks that do not produce a field enhancement at the upper antenna edge. Indeed, the field enhancement inside the nanocavity has been estimated to be on the order of 20–25× the incident field [23].

It is worth noting that the obtained absorption and enhancement values are particularly high considering that they originate from a single antenna. This can be attributed to the complex three-dimensional geometry of the system. The efficient excitation of higher order modes leads to intriguing consequences from the point of view of absorption and enhancement. In fact, it should be considered that broadband resonances are commonly correlated to efficient excitation and absorption over the spectrum, but bring about a poor electric field enhancement, which depends on the plasmon lifetime. As a general rule, it is possible to assume $\Delta\omega \approx \tau^{-1}$, where $\Delta\omega$ is the resonance width and τ is the plasmon lifetime, hence a narrower resonance implies a more efficient electric field accumulation [26]. This is not possible in common planar antennas, which usually present only a few lower order resonances along the two main axes, namely the longitudinal and the transverse ones [27]. As a result, in accordance with our previous work [23], the hollow nanocylinder shows a continuous extinction profile where individual resonances are independently excited, yet may no longer be resolved. This behavior also results in a remarkable field enhancement over the whole visible range, as shown in Figure 3a.

For the sake of clarity, Figure 3b reports the electric field distributions (along the antenna cross-section) only at λ = 514 and λ = 630 nm. In both cases, the presence of hotspots localized over the antenna's tip are clearly visible. These hotspots, together with the inner resonant modes (which give an addition-

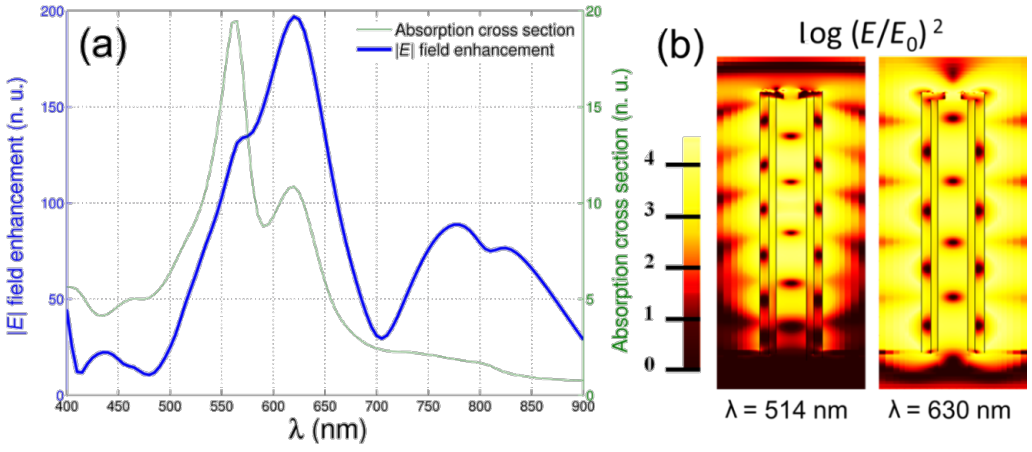

Figure 3: (a) Finite element method simulations of a silver nanotube with 1.4 µm height, 160 nm width, surface roughness of 4 nm and illuminated by TM polarized light impinging at 5°. The blue line represents the electric field enhancement calculated 1 nm above the upper antenna edge and normalized with respect to the impinging wave amplitude. The green line is the metal absorption cross section normalized to the incident power impinging on the antenna geometrical cross section. (b) Electric field maps corresponding to an excitation wavelength of 514 nm and 630 nm.

al contribution to the absorption), are correlated to the high electric field enhancement.

Evaluation through SERS effect

According to the calculations reported in Figure 3, the presence of an electromagnetic hotspot at the tip of the antenna leads to the assumption that the plasmonic properties of the antennas will present a specific distribution along the nanotube height. To confirm such a hypothesis, measurements of Raman scattering intensities of a monolayer of cresyl violet dye have been performed while changing the focussing distance of the collection objective (100×, focus depth <500 nm) from the substrate, and thus the focus along the *z* direction (antenna main axis).

To obtain a monolayer of dye, the sample was submerged into a solution of 1 μM cresyl violet for 5 min, allowing the dye molecules to be absorbed onto the metal surface. Then, the sample was rinsed in deionized water for 30 s to wash away excess molecules. The results of this experiment with an excitation wavelength of 633 nm are reported in Figure 4.

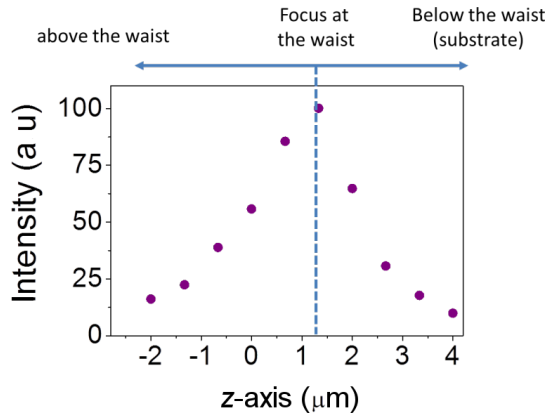

Figure 4: Measurements of Raman intensities along the *z*-axis of the antenna using cresyl violet dye.

Here, a strong dependence of the Raman intensity at a distance from the tip is visible. In particular, the graph presents a bell-shaped behavior, with a maximum value obtained when the focus is adjusted at the tip. Otherwise, for focal planes above or below the antenna, the Raman intensity shows a clear decrease. This result demonstrates that the majority of the Raman signal comes from the tip of the antenna and this can be attributed to the presence of the hotspot reported in Figure 3. In order to quantify the enhancement factor, we compared the Raman signal from the tip of an antenna with the signal coming from the surrounding silver substrate.

Figure 5 reports the Raman spectrum of the probe molecule absorbed on a single antenna at excitation wavelengths of λ = 514 and λ = 633 nm and the Raman spectrum obtained on the silver substrate close to the antenna (thickness 30 nm, local roughness 4 nm). The laser power and acquisition time were 1 μW and 1 s, respectively, for the spectra acquired on the antenna, and 10 μW and 50 s for that on substrate. The acquisition time and laser power are the same for the spectra acquired at λ = 514 nm and λ = 633 nm. The spectra intensities were normalized with respect to the most intense Raman peak (593 cm^{-1}).

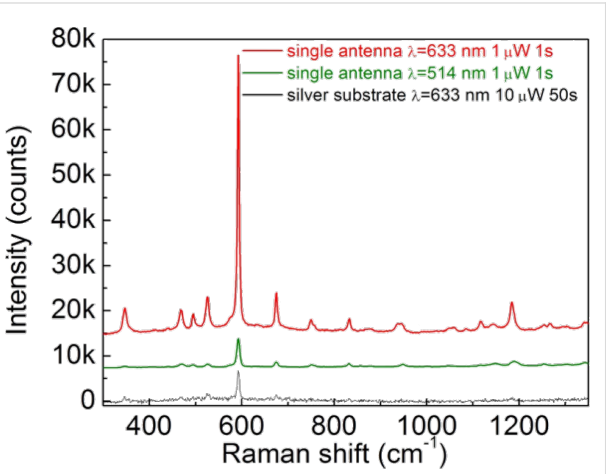

Figure 5: Raman scattering measurements of cresyl violet dye carried out on a rough silver substrate (black line) and single plasmonic nanoantenna (1.4 μm height and 80 nm radius) excited at a wavelength of λ = 633 nm (red line) and λ = 514 nm (green line).

Comparing the spectrum obtained on the antenna at λ = 633 nm (red line in Figure 5) with that on the substrate (black line in Figure 5), it is evident that the magnification of the Raman signals attributed to the antennas is much stronger than that of the silver film, thus confirming the effective capability of the hotspot at the antenna tip to act as field enhancer.

By taking into account the difference in laser power, integration time, signal counts, and number of scattering centers (hotspot area ≈10^3 nm^2, laser beam spot ≈2 × 10^6 nm^2) the estimated field enhancement factor of 60 was obtained. We remark that this value does not represent the absolute enhancement, but that one obtained in addition to that achievable on a rough silver surface. Since the latter is usually approximately 2–3 times the incident field or more, this implies that our antenna provides an experimental electromagnetic enhancement of about 120–180 in amplitude and is comparable to the result obtained by FEM calculations.

The data reported in Figure 5 allow quantification of the enhancement for a broadband wavelength range. Indeed, by comparing the spectral signals of the antennas, it is possible to

observe that the dye excited at λ = 514 nm exhibits intensities 9.4 times lower than that measured at λ = 633 nm. Since the Raman intensity depends on the 4^{th} power of the local electric field amplitude, this means that at λ = 514 nm a field amplitude enhancement of 1.75 times lower than the one provided at λ = 633 nm relates to an absolute pure electromagnetic enhancement of about 70–100 times the amplitude of incident field. If we consider other Raman peaks, this estimation gives even higher values (>100).

This behavior is in complete agreement with the results obtained by calculations as reported in Figure 3, exhibiting a broadband absorption and efficient enhancement of the electric field over a wide spectrum. According to FEM simulations, the value of the electric field at λ = 633 nm was 200 times higher with respect to the incident field, while at λ = 514 nm, this value decreased to a value of 100. This is 2 times lower than the that obtained at a resonant wavelength and comparable to the experimental value.

Furthermore, Raman experiments have demonstrated that even though the antennas were optimized to work at 633 nm, they also provide high amplification of the electromagnetic field at different wavelengths, and the resulting enhancement is still higher than that derived from conventional broad-range plasmonic enhancers, such as silver nanoparticles [28]. Moreover, it has been verified that a fine tuning of the optical properties of antennas can be achieved by controlling their geometrical parameters such as height and diameter, in accordance with calculations derived from the FEM method.

Experimental

Hollow three-dimensional electric field enhancing structures were obtained through an innovative fabrication method based on secondary electron lithography, generated by ion beam milling. The detailed process has been discussed elsewhere in depth [23]. Briefly, a layer of optical resist (Shipley S1813) is deposited by spin coating on the top of a silicon nitride membrane. The structure of the antenna is defined from the backside of the membrane by focused ion beam milling (FEI, NanoLab 600 dual beam system) using a gallium ion source with a current of 40 pA at a dose of 5 pC/μm^2. The interaction between gallium ions and the photoresist produces high secondary electrons doses, which cause the inversion of a thin layer of resist around the milled hole. When the sample is immersed in acetone, unexposed resist is dissolved while the exposed polymer is insoluble and remains attached to the membrane, representing an exact replica of the milled structure.

Finite element method simulations were performed using the software COMSOL Multiphysics.

Raman spectra were recorded with a Renishaw InVia spectrometer using 633 nm and 514 nm laser sources. The antenna excitation and signal acquisition were carried out through a 100× objective at normal incidence in reflection configuration.

Conclusion

In this work we demonstrated that engineered hollow plasmonic nanostructures can provide efficient electromagnetic field enhancement over a broadband spectrum. This could be a very attractive property for the design of highly versatile biosensors suitable for SERS spectroscopy on biological systems which use the entire visible wavelength range. The broadband enhancement feature is an addition to the already known broadband absorption of such systems [23].

FEM calculations were used to find suitable structure geometries by optimizing the value of electric field enhancement at 633 nm. It was found that a roughened silver nanoantenna presents an electric field enhancement value 200 times higher with respect to the incident field with respect to the optimal excitation wavelength. This value is far higher than values obtained for common plasmonic enhancers based on planar technologies.

In addition, hollow nanoantennas exhibit enhancement over a wide range of wavelengths – a feature not common in plasmonic systems. The simulation also revealed the presence of an electromagnetic field hotspot at the tip of the antenna confirmed by collecting the Raman spectra at different focusing distances along the main axis. A comparison of the Raman spectra obtained on antennas demonstrated an enhancement of the incident field of around 180 times. This was in accordance with the value calculated by FEM for the case of antennas excited on resonance and almost 2 times lower for out-of-resonance excitation. No consistent field enhancement was observed on the silver substrate close to antenna. These results are certainly encouraging and suggest the possibility of further integration of the nanocylinders in devices requiring multifunctional plasmonic properties over a broad wavelength range for the deep investigation of the complete cell environment.

Acknowledgments

The research leading to these results was funded by the European Research Council under the European Union's Seventh Framework Programme (FP/2007-2013)/ERC Grant Agreement number 616213, CoG: Neuro-Plasmonics.

References

1. Kennedy, D. C.; Tay, L.-L.; Lyn, R. K.; Rouleau, Y.; Hulse, J.; Pezacki, J. P. *ACS Nano* **2009,** *3,* 2329–2339. doi:10.1021/nn900488u

2. De Angelis, F.; Gentile, F.; Mecarini, F.; Das, G.; Moretti, M.; Candeloro, P.; Coluccio, M. L.; Cojoc, G.; Accardo, A.; Liberale, C.; Zaccaria, R. P.; Perozziello, G.; Tirinato, L.; Toma, A.; Cuda, G.; Cingolani, R.; Di Fabrizio, E. *Nat. Photonics* **2011,** *5,* 682–687. doi:10.1038/nphoton.2011.222
3. Huang, F. M.; Wilding, D.; Speed, J. D.; Russell, A. E.; Bartlett, P. N.; Baumberg, J. J. *Nano Lett.* **2011,** *11,* 1221–1226. doi:10.1021/nl104214c
4. Darvill, D.; Centeno, A.; Xie, F. *Phys. Chem. Chem. Phys.* **2013,** *15,* 15709–15726. doi:10.1039/c3cp50415h
5. Miele, E.; Malerba, M.; Dipalo, M.; Rondanina, E.; Toma, A.; De Angelis, F. *Adv. Mater.* **2014,** *26,* 4179–4183. doi:10.1002/adma.201400310
6. Homola, J. *Anal. Bioanal. Chem.* **2003,** *377,* 528–539. doi:10.1007/s00216-003-2101-0
7. Valsecchi, C.; Brolo, A. G. *Langmuir* **2013,** *29,* 5638–5649. doi:10.1021/la400085r
8. Choi, Y.; Kang, T.; Lee, L. P. *Nano Lett.* **2009,** *9,* 85–90. doi:10.1021/nl802511z
9. Smith, E. A.; Corn, R. M. *Appl. Spectrosc.* **2003,** *57,* 320A–340A. doi:10.1366/000370203322554446
10. De Angelis, F.; Das, G.; Candeloro, P.; Patrini, M.; Galli, M.; Bek, A.; Lazzarino, M.; Maksymov, I.; Liberale, C.; Andreani, L. C.; Di Fabrizio, E. *Nat. Nanotechnol.* **2010,** *5,* 67–72. doi:10.1038/nnano.2009.348
11. Srituravanich, W.; Durant, S.; Lee, H.; Sun, C.; Zhang, X. *J. Vac. Sci. Technol., B* **2005,** *23,* 2636–2639. doi:10.1116/1.2091088
12. Koenderink, A. F.; Hernández, J. V.; Robicheaux, F.; Noordam, L. D.; Polman, A. *Nano Lett.* **2007,** *7,* 745–749. doi:10.1021/nl0630034
13. Fang, Z.; Lin, C.; Ma, R.; Huang, S.; Zhu, X. *ACS Nano* **2010,** *4,* 75–82. doi:10.1021/nn900729n
14. Yin, L.; Vlasko-Vlasov, V. K.; Pearson, J.; Hiller, J. M.; Hua, J.; Welp, U.; Brown, D. E.; Kimball, C. W. *Nano Lett.* **2005,** *5,* 1399–1402. doi:10.1021/nl050723m
15. Bergman, D. J.; Stockman, M. I. *Phys. Rev. Lett.* **2003,** *90,* 027402. doi:10.1103/PhysRevLett.90.027402
16. Noginov, M. A.; Zhu, G.; Belgrave, A. M.; Bakker, R.; Shalaev, V. M.; Narimanov, E. E.; Stout, S.; Herz, E.; Suteewong, T.; Wiesner, U. *Nature* **2009,** *460,* 1110–1112. doi:10.1038/nature08318
17. Holmgaard, T.; Gosciniak, J.; Bozhevolnyi, S. I. *Opt. Express* **2010,** *18,* 23009–23015. doi:10.1364/OE.18.023009
18. Pile, D. F. P.; Gramotnev, D. K. *Opt. Lett.* **2005,** *30,* 1186–1188. doi:10.1364/OL.30.001186
19. Nazir, A.; Panaro, S.; Proietti Zaccaria, R.; Liberale, C.; De Angelis, F.; Toma, A. *Nano Lett.* **2014,** *14,* 3166–3171. doi:10.1021/nl500452p
20. Kneipp, K.; Kneipp, H.; Kneipp, J. *Acc. Chem. Res.* **2006,** *39,* 443–450. doi:10.1021/ar050107x
21. Notingher, I. *Sensors* **2007,** *7,* 1343–1358. doi:10.3390/s7081343
22. Li, M.; Xu, J.; Romero-Gonzalez, M.; Banwart, S. A.; Huang, W. E. *Curr. Opin. Biotechnol.* **2012,** *23,* 56–63. doi:10.1016/j.copbio.2011.11.019
23. De Angelis, F.; Malerba, M.; Patrini, M.; Miele, E.; Das, G.; Toma, A.; Zaccaria, R. P.; Di Fabrizio, E. *Nano Lett.* **2013,** *13,* 3553–3558. doi:10.1021/nl401100x
24. Gittard, S. D.; Nguyen, A.; Obata, K.; Koroleva, A.; Narayan, R. J.; Chichkov, B. N. *Biomed. Opt. Express* **2011,** *2,* 3167–3178. doi:10.1364/BOE.2.003167
25. Messina, G. C.; Wagener, P.; Streubel, R.; De Giacomo, A.; Santagata, A.; Compagnini, G.; Barcikowski, S. *Phys. Chem. Chem. Phys.* **2013,** *15,* 3093–3098. doi:10.1039/c2cp42626a
26. Fang, Z.; Thongrattanasiri, S.; Schlather, A.; Liu, Z.; Ma, L.; Wang, Y.; Ajayan, P. M.; Nordlander, P.; Halas, N. J.; de Abajo, F. J. G. *ACS Nano* **2013,** *7,* 2388–2395. doi:10.1021/nn3055835
27. Biagioni, P.; Huang, J.-S.; Hecht, B. *Rep. Prog. Phys.* **2012,** *75,* 024402. doi:10.1088/0034-4885/75/2/024402
28. Stratakis, E.; Kymakis, E. *Mater. Today* **2013,** *16,* 133–146. doi:10.1016/j.mattod.2013.04.006

License and Terms

BEILSTEIN JOURNAL OF NANOTECHNOLOGY

Synergic combination of the sol–gel method with dip coating for plasmonic devices

Cristiana Figus*[1], Maddalena Patrini[2], Francesco Floris[2], Lucia Fornasari[2], Paola Pellacani[3], Gerardo Marchesini[3], Andrea Valsesia[3], Flavia Artizzu[1,4], Daniela Marongiu[1], Michele Saba[1], Franco Marabelli[2], Andrea Mura[1], Giovanni Bongiovanni[1] and Francesco Quochi*[1]

Full Research Paper

Open Access

Address:
[1]University of Cagliari, Department of Physics, S.P. Monserrato-Sestu Km 0.7, 09042 Monserrato, Italy, [2]University of Pavia, Department of Physics, Via Agostino Bassi 6, 27100 Pavia, Italy, [3]Plasmore S.r.l., Via Grazia Deledda 4, 21020 Ranco, Italy and [4]University of Cagliari, Department of Chemistry and Geology, S.P. Monserrato-Sestu Km 0.700, 09042 Monserrato, Cagliari, Italy

Email:
Cristiana Figus* - cristiana.figus@dsf.unica.it; Francesco Quochi* - francesco.quochi@dsf.unica.it

* Corresponding author

Keywords:
biosensors; nanodevices; plasmonics; sol–gel; thin films

Beilstein J. Nanotechnol. **2015,** *6,* 500–507.
doi:10.3762/bjnano.6.52

Received: 10 September 2014
Accepted: 22 January 2015
Published: 19 February 2015

This article is part of the Thematic Series "Converging technologies for nanobio-applications".

Guest Editor: W. Lojkowski

Abstract

Biosensing technologies based on plasmonic nanostructures have recently attracted significant attention due to their small dimensions, low-cost and high sensitivity but are often limited in terms of affinity, selectivity and stability. Consequently, several methods have been employed to functionalize plasmonic surfaces used for detection in order to increase their stability. Herein, a plasmonic surface was modified through a controlled, silica platform, which enables the improvement of the plasmonic-based sensor functionality. The key processing parameters that allow for the fine-tuning of the silica layer thickness on the plasmonic structure were studied. Control of the silica coating thickness was achieved through a combined approach involving sol–gel and dip-coating techniques. The silica films were characterized using spectroscopic ellipsometry, contact angle measurements, atomic force microscopy and dispersive spectroscopy. The effect of the use of silica layers on the optical properties of the plasmonic structures was evaluated. The obtained results show that the silica coating enables surface protection of the plasmonic structures, preserving their stability for an extended time and inducing a suitable reduction of the regeneration time of the chip.

Introduction

Plasmonic nanostructures have gained increasing attention for their surface plasmon resonance (SPR)-related properties, which can be exploited in innovative technological applications. SPR is a phenomena arising from the interaction between the incident electromagnetic radiation and the conduction electrons present on a metal surface. Such coupling leads to an enhance-

ment and a spatial confinement of the electromagnetic field at a metal–dielectric interface [1-5]. Recently, due to such remarkable properties, biosensing technologies based on plasmonic nanostructures have attracted significant attention, particularly in the development of label-free sensors [6-8]. It is well known that surface plasmons (SPs) are extremely sensitive to the refractive index of the dielectric medium [1,2,9] and the two plasmons modes, surface plasmon polaritons (SPPs) and localized surface plasmons (LSPs), can be used for sensor applications [8,10,11].

However, in order to use this technology for sensing of a specific analyte, plasmonic-based devices require modifications of the metal surface that exceed some limitations of a bare metal surface [7,8]. The type of surface modification depends strongly on the application of the materials and can be achieved by various approaches [7,8,11,12]. Surface modification serves to stabilize the sensing platform (as in the case of metal nanoparticles) and provides a specific affinity, resulting in improved selectivity [7,8,11,12]. Furthermore, the surface chemistry of thiol-based self-assembled monolayers has shown some limitations mainly related to their temporal stability [13,14]. Therefore, research has been focus on the development of an ideal combination of surface functionalization methods and effective plasmonic structures for the detection and/or recognition of specific analytes.

However, independent from the considerations of the final application, sensing requires a chemically stable and optically tunable, dielectric platform, which should be properly functionalized: given these requirements, the silica layer coating represents a highly suitable method. However, the insertion of a silica layer between a plasmonic metal surface and a target molecule is not trivial. In fact, the electromagnetic field strength at a metal–dielectric interface decays exponentially from the metal surface [1,2,9]. Therefore, the proper deposition of a silica layer on the plasmonic structure is a critical factor since it can drastically reduce the action of the plasmonic field, due to the resulting increase in the distance from the metal surface. On the other hand, as demonstrated in our previous works, when the thickness of the silica layer is carefully controlled, a spatial redistribution with a consequent enhancement of the plasmonic field can be achieved [15,16]. However, a fine control of the layer thickness is also very important for plasmonic–photonic coupled devices [10,16-19].

For this purpose, the use of the sol–gel approach combined with the dip-coating technique to produce a silica layer is a suitable method for the modification of a plasmonic surface. In addition to preserving the nanostructured surface shape and its plasmonic action, this approach presents a proper platform for specific chemical functionalizations and, furthermore, it allows embedding of proper fluorophores and/or also specific molecules [20-22].

As previously mentioned a fine control of the layer thickness and of the matrix properties is critical. In this sense, many parameters affect the sol–gel mechanism reaction [23-26] and, therefore, the sol–gel process and the deposition technique should be optimized. To the best of our knowledge, few examples related to the use of a sol–gel approach for coating a planar nanostructure have been proposed in the literature [15-17,27]. Yet none of these works presented a comprehensive investigation of the effect of the key processing parameters.

The key processing parameters that allow for the fine-tuning of the silica layer thickness on a plasmonic structure were studied in this work. The plasmonic nanostructures were coated with conformal silica layers of controlled thickness using an optimized, combined sol–gel/dip-coating technique. The effects of the silica layer on the optical properties of the plasmonic nanostructure for sensing applications were investigated.

Results and Discussion

Silica coating control

In order to investigate the effect of the silica layer coating on the optical response of the plasmonic structure, the first step is to understand the role that the main parameters play on the layer thickness. Thus, the first goal was to prepare silica reference films and monitor their thickness as a function of various processing parameters, such as: pH, solvent concentration, aging time and withdrawal speed. These parameters play a significant role in the sol–gel mechanism reaction, affecting the microstructure homogeneity and the film thickness [23-27]. Moreover, a detailed optical study of the silica-coated plasmonic structure was performed.

The sol was prepared using tetraethoxysilane (TEOS) as a silica precursor, water at pH 1, 2, 3, 4 and 5, HCl (as a catalyst) and ethanol (EtOH). A water:TEOS molar ratio of five was used. The films were produced by dip-coating onto glass microscope slides with withdrawal speeds ranging from 0.6 to 1000 mm/min. The coated films were dried for 48 h at room temperature under ambient conditions. The thickness, refractive index and uniformity were evaluated and spectroscopic ellipsometry (SE) was employed as the main characterization technique to evaluate the film thickness. The film thickness was monitored as a function of different processing parameters, namely, pH, aging time, EtOH dilution, and withdrawal speed. The sol–gel process using silicon alkoxide precursors involves hydrolysis and condensation reactions, which lead to the formation of a silica network (Scheme 1) [23].

Hydrolysis

$$Si(OR)_4 + n\ H_2O \longrightarrow Si(OR)_{4-n}(OH)_n + n\ ROH$$

Water condensation

$$(RO)_3Si{-}OH + HO{-}Si(OR)_3 \longrightarrow (RO)_3Si{-}O{-}Si(OR)_3 + H_2O$$

Alcohol condensation

$$(RO)_3Si{-}OR + HO{-}Si(OR)_3 \longrightarrow (RO)_3Si{-}O{-}Si(OR)_3 + ROH$$

Scheme 1: Simplified sol–gel mechanism reaction for a tetraalkoxysilane [23].

Many processing parameters can affect the rate of hydrolysis and condensation, and thus, the features of the final material. Previous studies have reported the dependence of the sol–gel film thickness on the withdrawal speed, water:precursor molar ratio, and aging time [26,28-31]. However, all processing parameters must be controlled to carefully optimize the deposition onto the plasmonic nanostructures. In this study, a molar ratio of approximately 5 was used for all sols to favor a more complete hydrolysis and to produce more stable films [23,28-31].

Figure 1 shows the film thickness as a function of different processing parameters. Figure 1a shows a plot of the film thickness as a function of the withdrawal speed for films deposited on a bare glass substrate using a sol of starting pH ≈4 and few days of aging. In a matter similar to that previously observed by Faustini et al. [26], a critical withdrawal speed (≈50 mm/min) can be observed at which a minimum film thickness is achieved. In this regard, we note that the resulting films prepared at the critical speed of ≈50 mm/min are homogeneous, transparent and crack-free. The film thickness was also estimated using AFM with good agreement with the SE measurements.

The film thickness as a function of starting pH was also monitored. Figure 1b reports the film thickness obtained by keeping

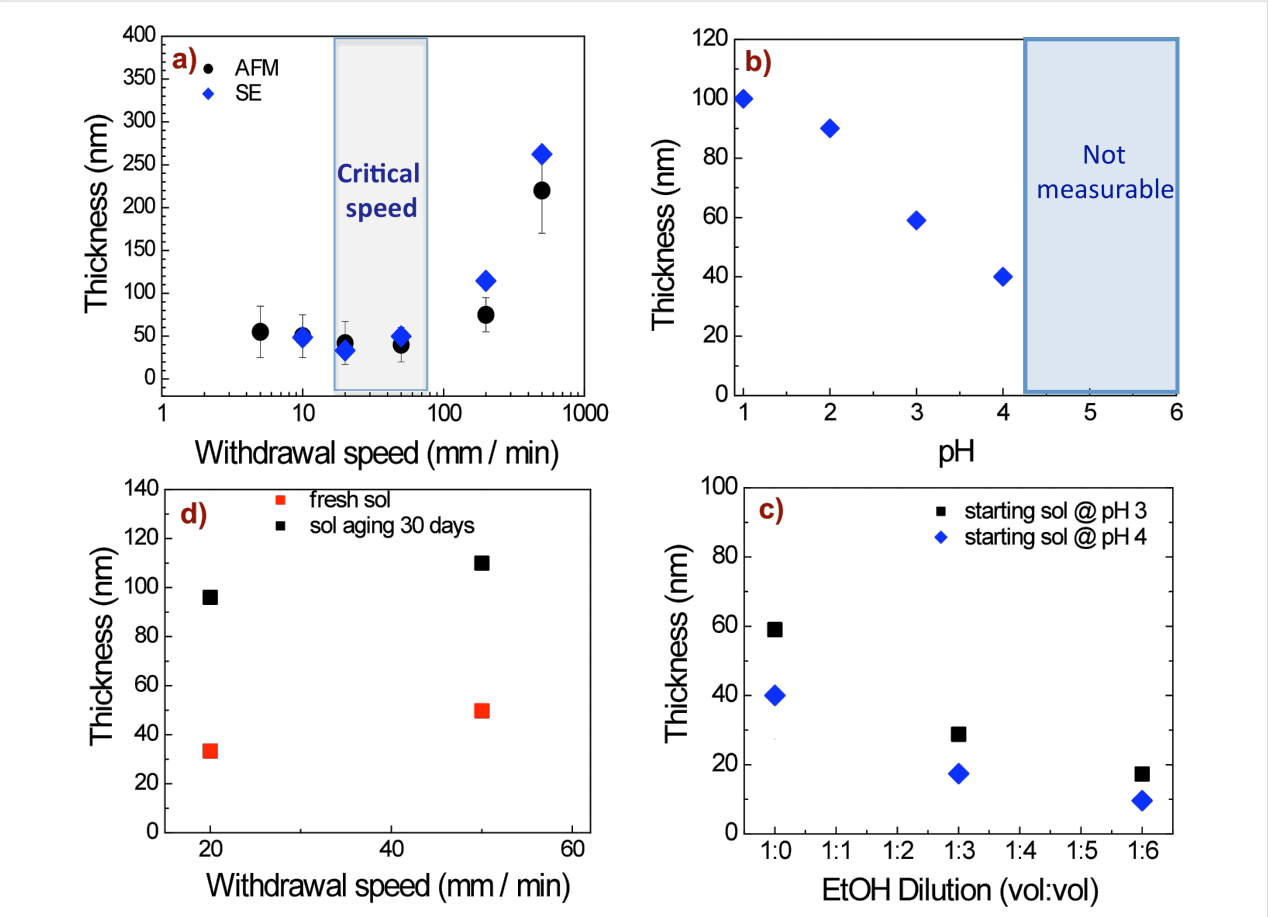

Figure 1: (a) Film thickness as a function of withdrawal speed for a sol of pH ≈4 and few days of aging, comparing results from both AFM and SE measurements. (b) Plot of the thickness versus starting pH value obtained at a withdrawal speed of 50 mm/min. (c) Plot of the thickness versus EtOH dilution at a withdrawal speed of 50 mm/min. (d) Plot of the thickness of a film prepared from fresh sol (starting pH ≈4) and from sol after 30 days.

the withdrawal speed fixed (50 mm/min), while using different starting pH values. A decrease in the thickness with increasing pH (until pH 4) can be observed. These results highlight that film thickness is strongly affected by pH. From the literature [28-31] it is known that the pH value affects the hydrolysis and condensation processes, and thus, it influences the morphology and structure of the resulting final material.

The film thickness, as expected [28-31] was also affected by aging time and dilution of the coating sol. Figure 1c,d shows the thickness of films prepared at a fixed withdrawal speed (50 mm/min) as a function of aging time (starting pH ≈4) and ethanol dilution (for two different starting pH values). The thickness decreases with the ethanol dilution (Figure 1c) and increases with the sol aging time (Figure 1d). According to the literature [26-29], the thickness is proportional to the sol viscosity; accordingly, it can be reduced by increasing the dilution since, which decreases the viscosity of the sol. On the other hand, when increasing the aging time, the viscosity increases, resulting in an increased thickness [23,28].

From the above data, the sol pH and dilution seem to have stronger effects on film thickness. These results were used as a calibration method to control the silica layer deposition on plasmonic structures. The film thickness was carefully tuned by controlling the pH and increasing the EtOH dilution of the sol, while operating at critical withdrawal speed. Specifically, for films prepared from fresh sol of pH ≈4 and 1:6 (v/v) EtOH dilution, a thickness less than 10 nm (Figure 1b,c) was reached. Therefore, the thickness of the silica films was controllable on the nanometer scale.

The control of the hydrophilic or hydrophobic property of the surface is an important characteristic from the perspective of biosensing applications since it also allows for altering the surface affinity for specific molecules. The surface of the films prepared from fresh sol of pH ≈4 was further characterized through contact angle measurements. As shown in Figure 2, these results highlight that the films are hydrophilic with a contact angle of 65°. This value is independent of the film thickness, but decreases with ethanol dilution up to 34° (inset of Figure 2). This suggests a correlation between the distribution of hydroxy groups, which affects film wettability, and the sol dilution. This change in the contact angle is probably due to the modification of the silica microstructure induced by an increase of the ethanol concentration, which is also supported by the decrease of the refractive index values for films prepared from diluted sols [28-31].

Figure 3 displays the refractive index, n, at the intermediate wavelength of 750 nm for silica layers of different thickness.

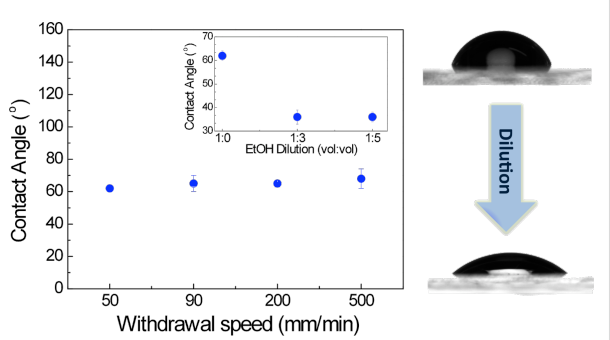

Figure 2: Contact angle measurements of a silica layer deposited by dip coating onto a glass substrate at different withdrawal speeds (left). Contact angle measurements of a silica layer deposited by dip coating at a 50 mm/min withdrawal speed onto a glass substrate as a function of ethanol dilution of the initial sol (right).

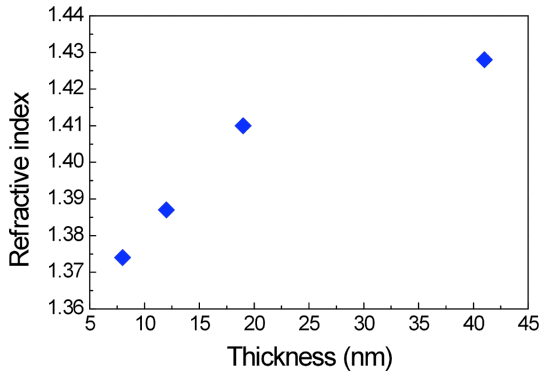

Figure 3: Refractive index, n, at 750 nm, evaluated by spectroscopic ellipsometry of silica layers deposited onto a glass substrate at a fixed withdrawal speed (50 mm/min) for different EtOH dilution (v/v = 1:0, 1:2, 1:4, 1:6).

The films were deposited onto a glass substrate at a fixed withdrawal speed (50 mm/s) for different EtOH dilutions (v/v = 1:0, 1:2, 1:4, 1:6) evaluated by SE.

Furthermore, the simultaneous analysis of SE data and transmittance spectra in the vis–NIR region were used to obtain the optical characteristics (n and the extinction coefficient, k) and to confirm the optical quality of the silica layers [15]. In particular, the SE measurements also indicate that the extinction coefficient is negligible through all the visible (vis) and near-infrared (NIR) range.

Coating of plasmonic structure

The results of the previous section were used as a calibration method to properly coat the surface of plasmonic devices consisting of a 2D array of truncated conical poly(methyl methacrylate) (PMMA) pillars [32-34]. Such a plasmonic platform has been shown to work efficiently as an SPR-sensitive

surface for biosensing applications in medical diagnostics [35]. A sketch of the pillar profile along a normal cross section is provided in Figure 4, where the procedure was adapted for silica layer deposition as schematically represented. The plasmonic structure is dipped in the sol and then withdrawn at a constant rate.

Figure 5 shows AFM topographies (performed in semi-contact mode) of the plasmonic structure before and after coating with a single layer of ≈6 nm and a double layer. The coatings were realized by using 1:6 (v/v) EtOH dilution of the starting sol (pH ≈4) at a withdrawal speed of 50 mm/min. The single layers were deposited by a single dip and the double layers were deposited by two dips (where the second layer was deposited 60 s after the first layer).

Conformal silica layers (i.e., those which maintain the original shape of the nanostructured surface) with a homogeneous coating was achieved, as is evidenced by the AFM topography after coating (Figure 5). The AFM images of the surface

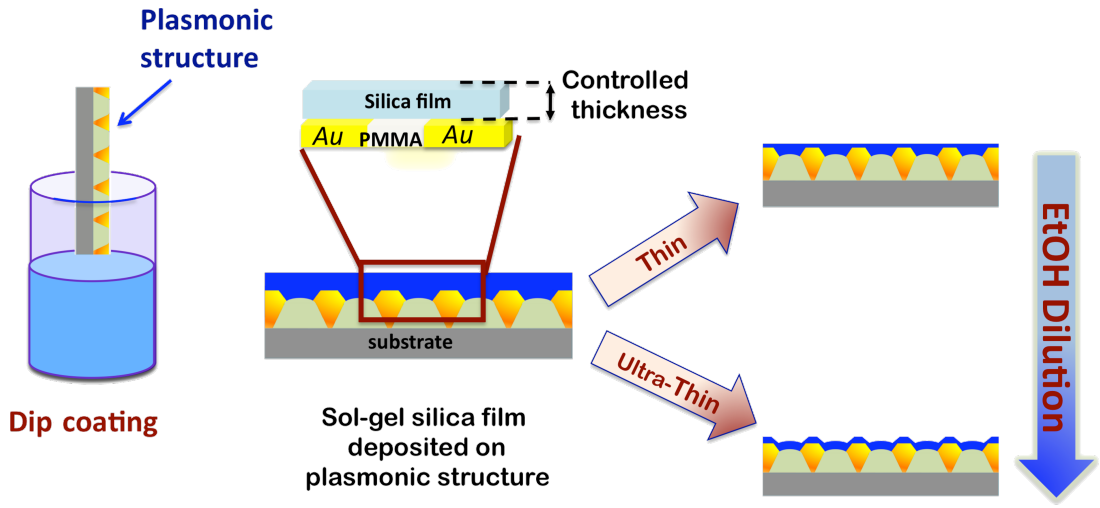

Figure 4: Tunable-thickness silica layer deposition onto plasmonic structures by dip coating. The thickness control of the layer is achieved by controlling pH, sol aging, withdrawal speed and the EtOH concentration.

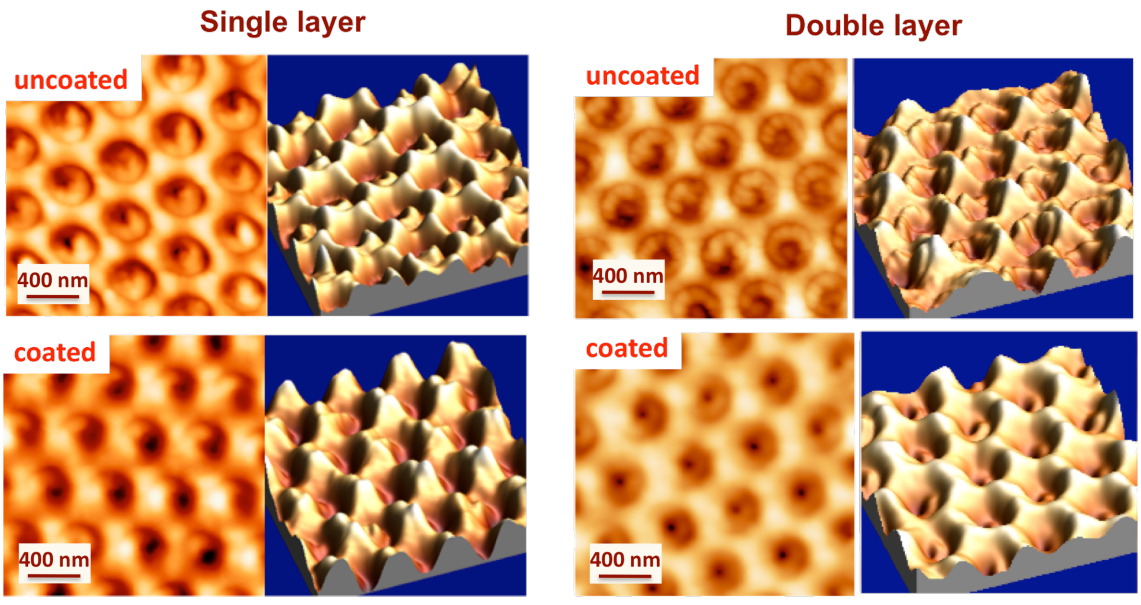

Figure 5: AFM topographies (semi-contact mode) and 3D morphological reconstruction of typical plasmonic structures before and after coating with a single layer of ≈6 nm (left) and a double layer (right) of silica. The coatings were realized by using 1:6 (v/v) EtOH dilution of the starting sol (pH ≈4) at a withdrawal speed of 50 mm/min.

reported in Figure 5 show the topography and the 3D morphological reconstruction of typical plasmonic structures before and after coating. A regular deposition of the pillars, with a hexagonal lattice structure, is clearly observed. Similar images were obtained for samples coated with layers of different thicknesses.

Effects of silica layer on plasmonic structures

The effect of using a silica-coated, plasmonic surface (optimized for biosensing) was analyzed by comparing the optical response before and after the coating process. The effects resulting from silica coating were assessed through the direct measurement of the sensitivity of the plasmonic structures to refractive index changes in aqueous solution. In the reflectance spectra, the plasmonic absorption feature is shifted to longer wavelengths due to the modification of the dielectric function surrounding the gold [1-4,15-17]. Figure 6 reports a simplified scheme showing the procedure used to perform the optical sensing test and to regenerate the sensor chip. The normalized reflectance spectra (R/R_0) of both a bare (uncoated), plasmonic, nanostructured chip and a chip coated with an ≈6 nm thick silica layer are shown. The reference reflectance spectrum (R_0, Figure 6a) is measured with the chip immersed in MilliQ water, and the reflectance spectrum (R, Figure 6c) is measured with the chip immersed in MilliQ water and EtOH (concentration, 3%). The optical response of the system was monitored through a series of measurements on the same solution (Figure 6, right) by evaluating the relative reflectance spectra (R/R_0) of the plasmonic, nanostructured surface coated with an ≈6 nm thick silica layer versus time. These results show that the use of silica layers leads to an improvement of the plasmonic surface protection. In particular, an easy reversibility and the reduction of the regeneration time of the chip (from 12 h to 30 min) was observed. Such a result is particularly interesting for the development of efficient, real-time sensors. Furthermore, we observe a clear improvement of the device sensitivity with respect to refractive index variations [15].

Moreover, the resulting silica sol–gel thin film behaved as a host matrix in which suitable vis or NIR fluorophore dopants could be dispersed. This is useful to couple the plasmonic and

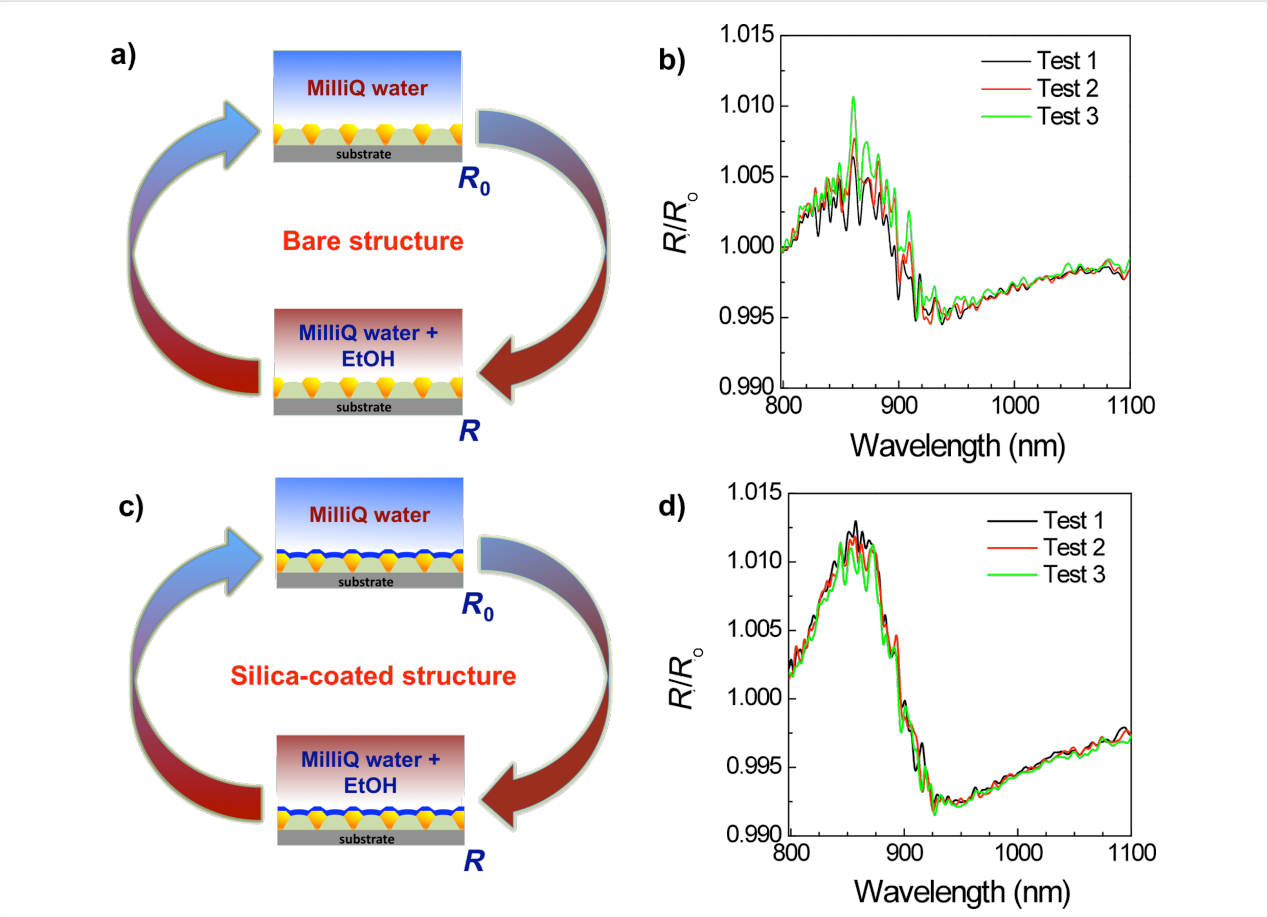

Figure 6: Simplified schemes showing the procedure used to perform the optical sensing and chip regeneration tests for (a) bare (uncoated) and (c) silica-coated structures. Normalized reflectance spectra (R/R_0) of a plasmonic, nanostructured chip for the (b) bare (uncoated) chip, tested with 12 h regeneration time and (d) an ≈6 nm thick silica layer coated chip, tested with 30 min regeneration times.

the emission signals, thus preventing undesirable metal-induced radiative emission quenching [17]. Finally, using organically modified alkoxides, the silica platform can be directly functionalized with selected functional groups required for specific detection schemes, all in a single-step process.

Conclusion

In this work, a combined optimized sol–gel method/dip-coating technique was exploited as a promising low-cost method for the realization of a silica-coated plasmonic platform with a high degree of silica thickness control. The key processing parameters that allow a fine-tuning of the silica layer thickness were investigated. This method enables modification of the nanostructure surface, while preserving the plasmonic functionality and broadening the potential of the plasmonic-based sensing applications. Indeed, such a sol–gel layer represents a proper framework to protect the plasmonic surface against external agents and reduces the sensor chip regeneration time. In addition, it represents a suitable platform to selectively bind target molecules with specific chemical functionalities through proper functionalization.

Experimental

Tetraethoxysilane (TEOS) with purity >99%, absolute ethanol (EtOH) with purity >99%, acetonitrile (MeCN) with purity >99% and distillated water (H_2O) were used as received without further purification. All reagents and solvents were purchased from Sigma-Aldrich. The sol precursor was prepared by mixing TEOS (8 mL), EtOH (20 mL) and H_2O (3.75 mL) under stirring at room temperature (RT) for 24 h. Subsequently, a volume of 6 mL of EtOH/MeCN (v/v = 1:1), and HCl (until pH 1, 2, 3, and 4 was reached) were added to 9 mL of the sol and the mixture was maintained under stirring at 50 °C for 1 h.

Additional diluted solutions were prepared by mixing a fresh TEOS solution with different amounts of EtOH (v/v = 1:0, 1:1, 1:2, 1:3, 1:4, 1:5, 1:6). The resulting diluted TEOS solutions were gently mixed in a closed vessel at RT. The molar ratio of water:precursor of the starting solution was 5 for all sols.

Soda-lime glass was employed as a substrate for reference film deposition. Before coating, the substrates were cleaned with water and soap, distilled water, acetone and finally, rinsed with isopropanol.

The films were deposited by dip coating at withdrawal speeds ranging from 0.01 to 20 mm/s. The glass substrates were immersed into the sol at a constant dipping speed of 8 mm/s and kept inside the bath for 25 s. After withdrawal, all films were dried at room temperature for 48 h.

The same method was used for coating the plasmonic structures. The single layers were deposited with one dip and the double layers were deposited with two dips (where the second layer was deposited after 60 s after the first layer).

The plasmonic structures were developed by Plasmore S.r.l. using colloidal lithography. They consisted of a 2D array of truncated, conical poly(methyl methacrylate) (PMMA) pillars (with a height of about 150 nm and a diameter of 350 nm) embedded into a gold layer that was used to fill the space between the pillars, resulting in a perforated-like film [32-35] .

An ND-R rotatory coater (Nadetech Innovations) was used for the deposition of all silica films.

An NT-MDT Solver-Pro AFM was used to analyze the topography and to estimate the thickness of the films. The measurements were performed at a scan speed of 0.5–1 Hz in semi-contact mode. In order to evaluate the film thickness using AFM, the fresh films deposited on the glass substrate were cut with a scalpel. After 48 h at room temperature, this cut on the film was observed by AFM for the thickness estimation. The evaluation of the surface roughness and thickness was performed by using WSxM 5.0 Develop3.2 software.

The wettability of the silica films was measured by using a Dataphysics Contact Angle System OCA, where a sessile drop method was used to measure the contact angle of a 5 µL distilled water droplet, which was applied to the surface by means of a syringe.

A variable angle SE (VASE, J. A. Woollam Co., Inc.) in the 0.25–2.5 µm wavelength range was used for the SE analysis, and an Agilent Cary 6000i spectrophotometer was used for normal-incidence reflectance and transmittance measurements in the 0.2–1.6 µm range.

The SE, reflectance and transmittance spectra were analyzed using dedicated WVASE32® software. Angle-resolved reflectance measurements were performed in the spectral range between 0.5 and 1.2 µm on the bare and coated plasmonic samples. This was made possible by a custom-built micro-reflectometer setup coupled to an FTIR (Bruker, IFS66).

Acknowledgements

The authors thank Regione Autonoma della Sardegna for financial support through POR Sardegna FSE L.R.7/2007 CRP-17571. C. F. acknowledges the Laboratory of Materials Science and Nanotechnology of the University of Sassari for the contact angle measurements.

References

1. Barnes, W. L. *J. Opt. A: Pure Appl. Opt.* **2006,** *8,* S87–S93. doi:10.1088/1464-4258/8/4/S06
2. Maier, S. A. *Plasmonics: Fundamentals and Applications;* Springer Science+Business Media LLC: New York, 2007.
3. Ma, R.-M.; Oulton, R. F.; Sorger, V. J.; Zhang, X. *Laser Photonics Rev.* **2013,** *7,* 1–21. doi:10.1002/lpor.201100040
4. Stewart, M. E.; Anderton, C. R.; Thompson, L. B.; Maria, J.; Gray, S. K.; Rogers, J. A.; Nuzzo, R. G. *Chem. Rev.* **2008,** *108,* 494–521. doi:10.1021/cr068126n
5. Bharadwaj, P.; Anger, P.; Novotny, L. *Nanotechnology* **2007,** *18,* 044017. doi:10.1088/0957-4484/18/4/044017
6. Anker, J. N.; Hall, W. P.; Lyandres, O.; Shah, N. C.; Zhao, J.; Van Duyne, R. P. *Nat. Mater.* **2008,** *7,* 442–453. doi:10.1038/nmat2162
7. Homola, J. *Chem. Rev.* **2008,** *108,* 462–493. doi:10.1021/cr068107d
8. Brolo, G. A. *Nat. Photonics* **2012,** *6,* 709–713. doi:10.1038/nphoton.2012.266
9. Barnes, W. L.; Dereux, A.; Ebbesen, T. W. *Nature* **2003,** *424,* 824–830. doi:10.1038/nature01937
10. Mayer, K. M.; Hafner, J. H. *Chem. Rev.* **2011,** *111,* 3828–3857. doi:10.1021/cr100313v
11. Szunerits, S.; Boukherroub, R. *Chem. Commun.* **2012,** *48,* 8999–9010. doi:10.1039/c2cc33266c
12. Jin, Y. *Adv. Mater.* **2012,** *24,* 5153–5165. doi:10.1002/adma.201200622
13. Love, J. C.; Estroff, L. A.; Kriebel, J. K.; Nuzzo, R. G.; Whitesides, G. M. *Chem. Rev.* **2005,** *105,* 1103–1170. doi:10.1021/cr0300789
14. Jans, K.; Bonroy, K.; De Palma, R.; Reekmans, G.; Jans, H.; Laureyn, W.; Smet, M.; Borghs, G.; Maes, G. *Langmuir* **2008,** *24,* 3949–3954. doi:10.1021/la703718t
15. Floris, F.; Figus, C.; Fornasari, L.; Patrini, M.; Pellacani, P.; Marchesini, G.; Valsesia, A.; Artizzu, F.; Marongiu, D.; Saba, M.; Mura, A.; Bongiovanni, G.; Marabelli, F.; Quochi, F. *J. Phys. Chem. Lett.* **2014,** *5,* 2935–2940. doi:10.1021/jz501443c
16. Floris, F.; Fornasari, L.; Patrini, M.; Figus, C.; Mura, A.; Bongiovanni, G.; Quochi, F.; Pellacani, P.; Valsesia, A.; Marabelli, F. *J. Phys.: Conf. Ser.* **2014,** *566,* 012015. doi:10.1088/1742-6596/566/1/012015
17. Figus, C.; Quochi, F.; Artizzu, F.; Saba, M.; Marongiu, D.; Floris, F.; Marabelli, F.; Patrini, M.; Fornasari, F.; Pellacani, P.; Valsesia, A.; Mura, A.; Bongiovanni, G. *AIP Conf. Proc.* **2014,** *1624,* 43–48. doi:10.1063/1.4900455
18. Fayyaz, S.; Tabatabei, M.; Hou, R.; Lagugne'-Labarthet, F. *J. Phys. Chem. C* **2012,** *116,* 11665–11670. doi:10.1021/jp302191z
19. Chen, Y.; Munechika, K.; Ginger, D. S. *Nano Lett.* **2007,** *7,* 690–696. doi:10.1021/nl062795z
20. Takahashi, M.; Figus, C.; Malfatti, L.; Tokuda, Y.; Yamamoto, K.; Yoko, T.; Kitanaga, T.; Tokudome, Y.; Innocenzi, P. *NPG Asia Mater.* **2012,** *4,* 22. doi:10.1038/am.2012.40
21. Sanchez, C.; Julián, B.; Belleville, P.; Popall, M. *J. Mater. Chem.* **2005,** *15,* 3559–3592. doi:10.1039/b509097k
22. Gupta, R.; Chaudhury, N. K. *Biosens. Bioelectron.* **2007,** *e22,* 2387–2399. doi:10.1016/j.bios.2006.12.025
23. Zha, J.; Roggendorf, H. In *Sol–gel science, the physics and chemistry of sol–gel processing;* Brinker, C. J.; Scherer, G. W., Eds.; Academic Press: Boston, 1990.
24. Innocenzi, P.; Figus, C.; Kidchob, T.; Takahashi, M. *J. Ceram. Soc. Jpn.* **2011,** *119,* 387–392. doi:10.2109/jcersj2.119.387
25. Innocenzi, P.; Figus, C.; Takahashi, M.; Piccinini, M.; Malfatti, L. *J. Phys. Chem. A* **2011,** *115,* 10438–10444. doi:10.1021/jp204314b
26. Faustini, M.; Louis, B.; Albouy, P. A.; Kuemmel, M.; Grosso, D. *J. Phys. Chem. C* **2010,** *114,* 7637–7645. doi:10.1021/jp9114755
27. Yasukuni, R.; Ouhenia-Ouadahi, K.; Boubekeur-Lecaque, L.; Félidj, N.; Maurel, F.; Méltivier, R.; Nakatani, K.; Aubard, J.; Grand, J. *Langmuir* **2013,** *29,* 12633–12637. doi:10.1021/la402810e
28. McDonagh, C.; Sheridan, F.; Butler, T.; MacCraith, B. D. *J. Non-Cryst. Solids* **1996,** *194,* 72–77. doi:10.1016/0022-3093(95)00488-2
29. Brinker, C. J.; Hurd, A. J.; Schunk, P. R.; Frye, G. C.; Ashley, C. S. *J. Non-Cryst. Solids* **1992,** *147–148,* 424–436. doi:10.1016/S0022-3093(05)80653-2
30. Xiao, Y.; Shen, J.; Xie, Z.; Zhou, B.; Wu, G. *J. Mater. Sci. Technol.* **2007,** *23,* 504–508.
31. Tamar, Y.; Tzabari, M.; Haspel, C.; Sasson, Y. *Sol. Energy Mater. Sol. Cells* **2014,** *130,* 246–256. doi:10.1016/j.solmat.2014.07.020
32. Giudicatti, S.; Marabelli, F.; Valsesia, A.; Pellacani, P.; Colpo, P.; Rossi, F. *J. Opt. Soc. Am. B* **2012,** *29,* 1641–1647. doi:10.1364/JOSAB.29.001641
33. Giudicatti, S.; Valsesia, A.; Marabelli, F.; Colpo, P.; Rossi, F. *Phys. Status Solidi A* **2010,** *207,* 935–942. doi:10.1002/pssa.200925579
34. Giudicatti, S.; Marabelli, F.; Pellacani, P. *Plasmonics* **2013,** *8,* 975–981. doi:10.1007/s11468-013-9499-9
35. Bottazzi, B.; Fornasari, L.; Frangolho, A.; Giudicatti, S.; Mantovani, A.; Marabelli, F.; Marchesini, G.; Pellacani, P.; Therisod, R.; Valsesia, A. *J. Biomed. Opt.* **2014,** *19,* 017006. doi:10.1117/1.JBO.19.1.017006

License and Terms

BEILSTEIN JOURNAL OF NANOTECHNOLOGY

Low-cost formation of bulk and localized polymer-derived carbon nanodomains from polydimethylsiloxane

Juan Carlos Castro Alcántara, Mariana Cerda Zorrilla, Lucia Cabriales, Luis Manuel León Rossano and Mathieu Hautefeuille*

Full Research Paper

Open Access

Address:
Departamento de Física Facultad de Ciencias, Universidad Nacional Autónoma de México, Avenida Universidad 3000, Circuito Exterior S/N, Delegación Coyoacán, C.P. 04510 Ciudad Universitaria, D.F. México, México

Email:
Mathieu Hautefeuille* - mathieu_h@ciencias.unam.mx

* Corresponding author

Keywords:
carbon nanodomains; nanodots; polydimethylsiloxane; polymer-derived ceramics; Raman spectroscopy

Beilstein J. Nanotechnol. **2015,** *6,* 744–748.
doi:10.3762/bjnano.6.76

Received: 30 June 2014
Accepted: 18 February 2015
Published: 16 March 2015

This article is part of the Thematic Series "Converging technologies for nanobio-applications".

Guest Editor: W. Lojkowski

Abstract

We present two simple alternative methods to form polymer-derived carbon nanodomains in a controlled fashion and at low cost, using custom-made chemical vapour deposition and selective laser ablation with a commercial CD-DVD platform. Both processes presented shiny and dark residual materials after the polymer combustion and according to micro-Raman spectroscopy of the domains, graphitic nanocrystals and carbon nanotubes have successfully been produced by the combustion of polydimethylsiloxane layers. The fabrication processes and characterization of the byproduct materials are reported. We demonstrate that CVD led to bulk production of graphitic nanocrystals and single-walled carbon nanotubes while direct laser ablation may be employed for the formation of localized fluorescent nanodots. In the latter case, graphitic nanodomains and multi-wall carbon nanotubes are left inside microchannels and preliminary results seem to indicate that laser ablation could offer a tuning control of the nature and optical properties of the nanodomains that are left inside micropatterns with on-demand geometries. These low-cost methods look particularly promising for the formation of carbon nanoresidues with controlled properties and in applications where high integration is desired.

Introduction

Silicon-based polymer-derived ceramics (PDC) are of increasing interest thanks to the relatively controlled production and recent utilization of their unique functional properties. Their great resistance and stability to high temperatures, chemical durability or semiconducting behaviour are indeed permitting new applications as catalysis supports, highly resistant materials for aerospace and automotive industry, microelectronics, optics and even biotechnology [1]. Recent efforts have been

made to properly control and characterize the production of various forms of PDC pyrolysing different preceramic polymers. Coatings, fibres and orderly porous components may then be obtained according to the desired application and nanodomains such as carbon nanotubes and nanowires, silicon carbide (SiC) and SiC/SiO2 nanofibres have also been recently produced [2,3]. Typically, the use of special fillers and high temperatures of 1000 °C or greater are critical for the kinetics, morphology, composition and organization of the resulting residual nanostructures. Moreover, the complex nature of preceramic silicon-based polymers may also represent a limitation to the formation of PDC nanodomains. It has been reported that carbon nanostructures may be obtained through the chemical vapour deposition (CVD) technique by using alcohols as reagent for carbon sources. For instance, aliphatic alcohols or mixtures of ethanol and methanol with other substances such as ferrocenes may also be used, depending on the type of the desired carbon nanodomains [4,5]. Laser pyrolysis may also be used to produce PDC in a rapid, local and selective fashion, although it is less common than CVD due its non-continuous work regime limiting the process [1]. Recently, a high power ultraviolet laser has been employed to directly induce the localized formation of nanocrystalline silicon residues in a low-cost polymer matrix with many interesting properties in optics and electronics micro-integration: polydimethylsiloxane (PDMS) [6].

In this work, we report the formation of bulk or localized carbon nanodomains obtained from PDMS, a silicon-based polymer by using two different methods enabled by low-cost custom-made platforms: chemical vapour deposition at 900 °C and selective laser ablation (SLA). In both procedures, it has been found that the combustion of PDMS successfully formed residual nanomaterials of different compositions and ordering depending on the formation conditions. Ease of use at atmospheric pressure and low cost are characteristics of the two alternative techniques employed here for PDC nanodomains production. In CVD, the evaporation of the reagent over the PDMS at high temperatures allowed for the rearrangement of carbon structures in PDMS to produce two layers composed of two different carbon structures. In the case of SLA, a continuous-wave infrared laser beam was focused on the surface of PDMS membranes coated with a thin layer of absorbing carbon nanopowder. This generates superficial laser-induced incandescence and forms highly localized carbon nanodomains inside the microscopic volume of etched material [7]. In this particular case, the PDC organization was highly dependent on lasing conditions and the process proved to be useful to produce localized fluorescent nanodomains in a PDMS matrix with a direct, controlled, rapid-prototyping method, similar to other SLA methods [8].

Results and Discussion

Chemical vapour deposition

When a commercial CVD reactor is lacking, the low-cost alternative constructed here using conventional laboratory materials showed to be capable of vapour deposition at atmospheric pressure. The setup consists of three essential parts: reagents evaporation stage, deposition chamber and residual gases expulsion stage, as shown in Figure 1. The reagents evaporation is based on a heating system and a glass recipient connected to the deposition chamber through a valve. The deposition chamber consists of a quartz tube located inside a muffle (Lindberg 51894), sealed by a two-hole rubber stopper that allows for gas transport both inwards and outwards. Residual gases expulsion is verified by their bubbling in a water container placed outside the chamber.

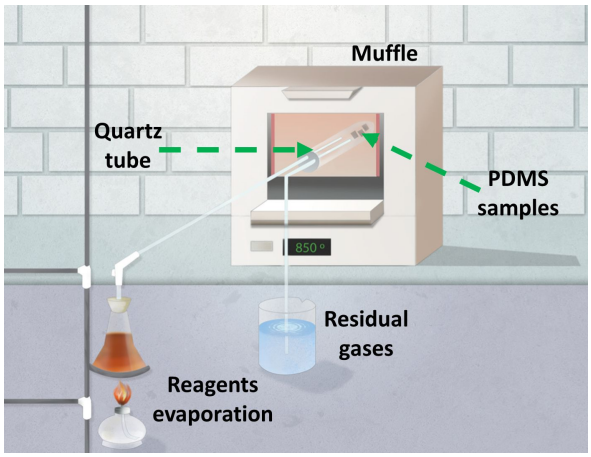

Figure 1: Diagram of the custom-made atmospheric pressure CVD reactor.

The reagent used in this work for nanodomains production was a solution of ethanol (laboratory reagent purchased from Sigma-Aldrich, Part No. 16368) in water at 43% (v/v). The 3 mm thick PDMS layers on which it was evaporated were prepared from a Sylgard 184 kit (purchased from Dow Corning) mixing the pre-polymer with its curing agent in a 10:1 weight proportion following the conventional procedure. The gel was then deposited on clean glass substrates and cured at 90 °C for 2 h in a convection oven before they were detached and stored in hermetic containers. Vapour deposition of the reagent was performed at 900 °C over one hour and temperature was measured with a type-K thermocouple placed inside the deposition chamber. A post-treatment consisting in heating the sample at the same temperature for 30 min has been implemented to improve deposition and ordering of the structures [9]. After this procedure, the quartz tube was removed to let the chamber cool

down to ambient temperature and the samples were carefully extracted with tweezers due to their brittle nature.

Two very distinct types of residual layers were always observed after the CVD procedure: dark and shiny layers have been obtained in a highly repeatable manner under the previously described particular conditions (Figure 2). Different geometries and shapes have been used and it did not affect the results. The totality of the pristine PDMS layers was then transformed into these two layers, proving that this method is appropriate for bulk production of these residues. The Raman spectra of these optically different materials, obtained with a Raman microscope with a 532 nm laser of (Thermo Scientific DXR), showed that the layers obtained with the CVD technique are very different from that of a pristine PDMS substrate, as seen in Figure 2. In both cases, the D (ca. 1350 cm^{-1}) and G (ca. 1598 cm^{-1}) bands, characteristics of carbon materials, are clearly present. However, the G′ band (ca. 2700 cm^{-1}) is visible in the dark regions while the 2D band (ca. 2700 cm^{-1}) and the G + D band (ca. 2935 cm^{-1}) are characteristics of the shiny areas [10]. The difference in visual appearance may then be also justified by a shift between these bands intensities, identifying distinct structures at nanoscale for each of the residual materials. Indeed, according to the literature [11-13], the greater intensity of the D band with respect to the G band and the presence of the RBM band (ca. 270 cm^{-1}) demonstrate that graphitic nanocrystals (GNC) are composing the shiny layers, whereas dark parts consist mainly of single-walled carbon nanotubes (SWCNT) [14].

Selective laser ablation

Selective and localized laser pyrolysis has also been tested to study the formation of nanodomains from PDMS in a controlled fashion, using a low-cost technique that allows laser micropattern formation in PDMS [15]. The setup used to locally etch polymer layers at the surface is based on a commercial CD-DVD optical pickup unit (OPU) mounted on a controllable platform [15]. It also allows for the precise control of laser power density and dwell time to control the formation of nanodomains. In spite of PDMS transparency at OPU available wavelengths, laser ablation has been achieved by coating the cured PDMS surface with absorbing carbon nanopowder clusters (Sigma-Aldrich, Part No. 633100) and focusing the infrared beam (785 nm) onto it above a certain power density threshold to generate localized laser-induced incandescence. The elevated heat generated by this phenomenon at the surface of PDMS is sufficient to generate a microplasma that promotes the combustion of the silicon-based elastomer and removes a microscopic volume of the polymer. Under certain controllable conditions, the combustion produces fumes and leaves black, fluorescent residual materials inside the resulting etched patterns [15]. Finally, the etched volumes are cleaned by using distilled water or common organic solvents that do not dissolve nor swell PDMS and remove additional nanopowders.

The SLA process produced nanocarbon residues inside micron-scale laser-etched PDMS channels with on-demand geometry. Dark and shiny domains were also observed by using polarized-light microscopy during which it was evidenced that the laser formation of the nanodomains is extremely localized. This has been clearly identified by the presence of fluorescent compounds inside the channels. The composition of the combustion residues has been characterized first with a NORAN energy dispersive X-ray spectroscopy (EDX) system working at 20 keV in a scanning electron microscope (Jeol JSM-5600LV). The EDX analysis showed that residues are mainly silicon and oxygen, in similar weight proportions, and that carbon is only present in regions etched at the greatest laser intensities. In this

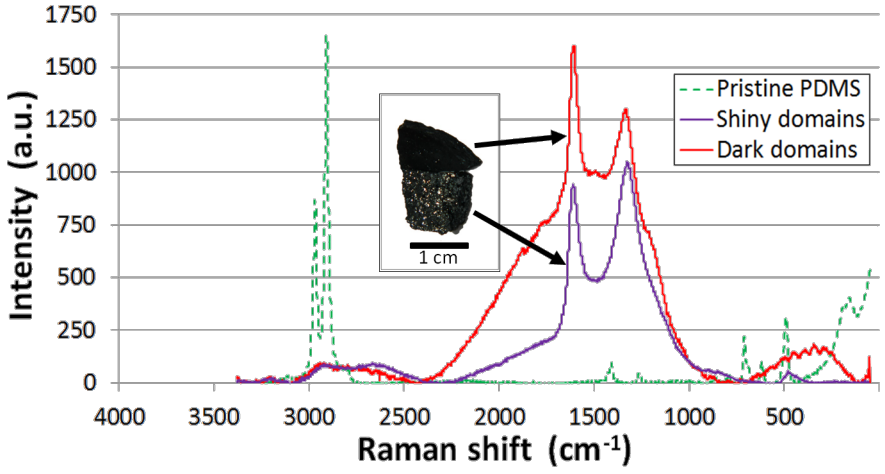

Figure 2: Comparison of Raman spectra: pristine PDMS, carbon nanotubes (shiny domains) and graphite nanocrystals (dark domains).

case, 47.5% oxygen, 29.3% silicon and 23.2% carbon are found inside the channels demonstrating that greater temperatures reached during incandescence produce carbon nanodomains locally.

The composition of the residues was then studied with Raman spectroscopy (Figure 3). This characterization showed residual materials structures inside microchannels similar to what was found after bulk PDC formation by using the CVD method. Namely, graphitic nanocrystals were found in shiny areas (demonstrated by the presence of D, G and 2D bands) while multi-wall carbon nanotubes (MWCNT) were found in dark regions (with the apparition of D, G and G′ bands, but without RBM band) [16]. It is interesting to remark that the laser-etched residual materials are slightly different from those obtained from CVD. No silicon oxides have been observed either, although it has been reported that they are typical residues of PDMS combustion [17]. This absence could be explained by the thermal conditions for PDMS ablation, since factors such as transient and final temperature during laser exposure greatly influence the nature of the byproducts as described in [17-19]. It has also been observed that the organization of carbon nanodomains is greatly affected by laser power density, thus by the temperature caused by the nanocarbon absorption of laser light (Figure 3b). This seems to indicate that the thermal conditions also play an important role in the nature of this type of byproducts [19]. Although the temperature reached on the PDMS surface has not been measured, the control of lasing conditions offered high process repeatability to obtain carbon nanodomains in a controlled fashion and with greater order than those obtained with a high-power excimer laser [6]. This shows that further work is needed in monitoring and controlling the thermal parameters of our SLA process. Finally, fluorescence has been observed inside the etched channels and it has been shown that its intensity is very much dependent on the laser power density used to etch the patterns, as described earlier in [15]. As fluorescence is visible after cleaning the samples, some nanoresidues are clearly embedded inside the polymer matrix, similar to what is reported in [20]. The nanoresidues also show good photothermal stability as the intensity of the fluorescence emission did not present quenching after hours of irradiation under a fluorescence microscope or when characterized with a 4 W UV lamp and characterized with a photomultiplier tube, even months after their formation. Unfortunately, the dependence of the fluorescence wavelengths and surface chemistry of the nanodomains with laser conditions as well as the thermal conditions influence on nanodomains formation have not been studied and will require future work to address these important parameters and to verify if our methods can be a low-cost solution for the tunable formation of carbon nanodots.

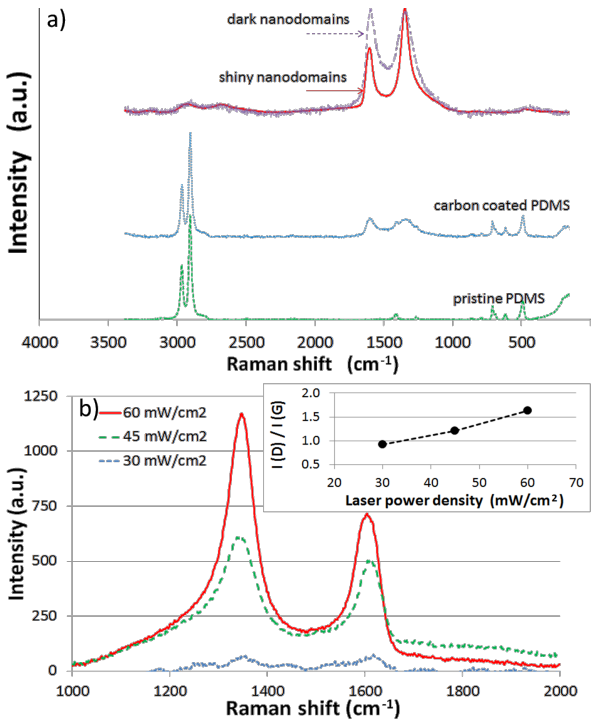

Figure 3: Raman characterization spectra of pristine PDMS, coated PDMS and residual nanodomains of shiny and dark domains in etched channels after cleaning (a). Influence of laser power density on G and D bands intensities (b).

Acknowledgements

The authors would like to thank Cristina Zorrila Cangas (Laboratorio de Materiales Avanzados, IF-UNAM) for technical help in Raman spectroscopy.

References

1. Colombo, P.; Mera, G.; Riedel, R.; Sorarù, G. D. *J. Am. Ceram. Soc.* **2010,** *93,* 1805–1837. doi:10.1111/j.1551-2916.2010.03876.x
2. Berger, A.; Pippel, E.; Woltersdorf, J.; Scheffler, M.; Cromme, P.; Greil, P. *Phys. Status Solidi A* **2005,** *202,* 2277–2286. doi:10.1002/pssa.200521201
3. Lu, P.; Huang, Q.; Mukherjee, A.; Hsieh, Y.-L. *J. Mater. Chem.* **2011,** *21,* 1005–1012. doi:10.1039/c0jm02543g
4. Chaisitsak, S.; Nukeaw, J.; Tuantranont, A. *Diamond Relat. Mater.* **2007,** *16,* 1958. doi:10.1016/j.diamond.2007.09.013
5. Liu, Y.; Tzeng, Y.; Tso, P.; Lin, I. Nanocrystalline diamond films deposited by microwave plasma CVD in mixtures of argon and methane with and without hydrogen additive. In *Proceedings of the Seventh Applied Diamond Conference/Third Frontier Carbon Technology Joint Conference, ADC/FCT 2003,* Tsukuba, Japan, Aug 18–21, 2003; p 547.
6. Dupas-Bruzek, C.; Robbe, O.; Addad, A.; Turrell, S.; Derozier, D. *Appl. Surf. Sci.* **2009,** *255,* 8715–8721. doi:10.1016/j.apsusc.2009.06.025
7. Lim, Z. H.; Lee, A.; Zhu, Y.; Lim, K.-Y.; Sow, C.-H. *Appl. Phys. Lett.* **2009,** *94,* 073106. doi:10.1063/1.3083554

8. Friedel, T.; Travitzky, N.; Niebling, F.; Scheffler, M.; Greil, P. *J. Eur. Ceram. Soc.* **2005,** *25,* 193–197. doi:10.1016/j.jeurceramsoc.2004.07.017
9. Law, M.; Luther, J. M.; Song, Q.; Hughes, B. K.; Perkins, C. L.; Nozik, A. J. *J. Am. Chem. Soc.* **2008,** *130,* 5974–5985. doi:10.1021/ja800040c
10. Jorio, A. *ISRN Nanotechnol.* **2012,** No. 234216. doi:10.5402/2012/234216
11. Jerng, S. K.; Yu, D. S.; Kim, Y. S.; Ryou, J.; Hong, S.; Kim, C.; Yoon, S.; Efetov, D. K.; Kim, P.; Chun, S. H. *J. Phys. Chem. C* **2011,** *115,* 4491. doi:10.1021/jp110650d
12. Bokobza, L.; Zhang, J. *eXPRESS Polym. Lett.* **2012,** *6,* 601. doi:10.3144/expresspolymlett.2012.63
13. Hodkiewicz, J. Thermo Fisher Scientific Application Note: 51901.
14. Graupner, R. *J. Raman Spectrosc.* **2007,** *38,* 673. doi:10.1002/jrs.1694
15. Hautefeuille, M.; Cabriales, L.; Pimentel-Domínguez, R.; Velázquez, V.; Hernández-Cordero, J.; Oropeza-Ramos, L.; Rivera, M.; Carreón-Castro, M. P.; Grether, M.; López-Moreno, E. *Lab Chip* **2013,** *13,* 4848–4854. doi:10.1039/c3lc51041g
16. Grassi, G.; Scala, A.; Piperno, A.; Iannazzo, D.; Lanza, M.; Milone, C.; Pistone, A.; Galvagno, S. *Chem. Commun.* **2012,** *48,* 6836–6838. doi:10.1039/c2cc31884a
17. Genovese, A.; Shanks, R. A. *Composites, Part A* **2008,** *39,* 398–405. doi:10.1016/j.compositesa.2007.09.009
18. Camino, G.; Lomakin, S. M.; Lageard, M. *Polymer* **2002,** *43,* 2011–2015. doi:10.1016/S0032-3861(01)00785-6
19. Lewicki, J. P.; Liggat, J. J.; Patel, M. *Polym. Degrad. Stab.* **2009,** *94,* 1548–1557. doi:10.1016/j.polymdegradstab.2009.04.030
20. Usman Zillohu, A.; Abdelaziz, R.; Keshavarz Hedayati, M.; Emmler, T.; Homaeigohar, S.; Elbahri, M. *J. Phys. Chem. C* **2012,** *116,* 17204–17209. doi:10.1021/jp3016358

License and Terms